Ketogenic Diet Induces Anti-Tumorigenic Effects in Colorectal Cancer through Microbial Production of Stearate

Mina Tsenkova[1], Madita Brauer[1,2], Marat Kasakin[3], Susheel Bhanu Busi[3,4], Maryse Schmoetten[1], Anthoula Gaigneaux[5], Vitaly Pozdeev[1], Marianne Meyers[1], Eric Koncina[1], Diran Herebian[6], Fabien Rodriguez[1], Dean Cheung[1], Martine Schmitz[1], Laura de Nies[3], Ertan Mayatepek[6], Serge Haan[1], Carine de Beaufort[7], Jérôme Graas[8], Thorsten Cramer[9], Carole L. Linster[3], Paul Wilmes[3,5], Elisabeth Letellier[1]

[1] Molecular Disease Mechanisms Group, Department of Life Sciences and Medicine, Faculty of Science, Technology and Medicine, University of Luxembourg, Esch-sur-Alzette, Luxembourg

[2] Institute for Advanced Studies, University of Luxembourg, Esch-sur-Alzette, Luxembourg

[3] Luxembourg Centre for Systems Biomedicine, University of Luxembourg, Esch-sur-Alzette, Luxembourg

[4] UK Centre for Ecology and Hydrology, Wallingford, United Kingdom

[5] Department of Life Sciences and Medicine, Faculty of Science, Technology and Medicine, University of Luxembourg, Esch-sur-Alzette, Luxembourg

[6] Department of General Pediatrics, Neonatology and Pediatric Cardiology, Medical Faculty and University Hospital Düsseldorf, Heinrich Heine University, Düsseldorf, Germany

[7] Pediatric Clinic, Centre Hospitalier de Luxembourg, Luxembourg, Luxembourg

[8] Centre d'Investigation et d'Epidémiologie Clinique, Luxembourg Institute of Health, Hesperange, Luxembourg

[9] Molecular Tumor Biology, Department of General, Visceral and Transplantation Surgery, RWTH University Hospital Aachen, Germany

Abstract

Colorectal cancer (CRC) patients have been shown to possess an altered gut microbiome. Diet is a known microbiome modulator. An attenuating effect of the ketogenic diet (KD) on CRC cell growth has been previously observed, however the role of the gut microbiome in driving this effect remains unknown. Here, we describe a reduced colonic tumor burden upon KD consumption in a CRC mouse model with a humanized microbiome. Importantly, we demonstrate a causal relationship through microbiome transplantation into germ-free mice, whereby alterations in gut microbial function were maintained in the absence of continued selective pressure from the KD. We identify stearic acid as a putative microbiome-derived anti-cancer metabolite. Taken together, the beneficial effects of the KD are mediated by the gut microbiome and may be dependent on a pre-existing “non-responder” or “responder” gut microbiome profile. These results have important implications for future clinical trials evaluating the effects of the ketogenic diet on human CRC.

43 **Introduction**

44 Worldwide, colorectal cancer (CRC) is the third most prevalent cancer, with over 1.9 million new
45 cases recorded in 2020[1]. CRC incidence and mortality rates have been associated with various lifestyle-
46 related risk factors, in particular dietary habits. Recent years have seen a rise in CRC incidence in persons
47 aged 50 years and under, further underlining the importance of studying these factors[2]. The ketogenic
48 diet (KD) has been shown to possess anti-cancer properties in the context of CRC, and many studies have
49 focused on the importance of the restriction of energy to slow the growth of rapidly proliferating cells and
50 anti-cancer signaling through ketone bodies[3]. One recently published study investigated the effects of the
51 KD on CRC development and described a new mechanism through which KD exerts its anti-cancer effects,
52 namely through the ketone body β-hydroxybutyrate acting on the surface receptor Hcar2, inducing the
53 transcriptional regulator *Hopx*, thus altering gene expression and inhibiting cell proliferation[4]. These
54 studies often focus on the effects of KD on the cancer cells themselves, and rarely on other cells of the
55 tumor microenvironment (TME), such as immune cells[5,6] and cancer-associated fibroblasts (CAFs)[7], or on
56 external factors, such as the gut microbiome. Specifically in CRC, cancer progression is accompanied by a
57 state of dysbiosis of the gut microbiome[8–10]. The study of the role of the different bacteria in CRC is of
58 particular interest, considering the affected tissue type is in contact with the gut microbiome. Until
59 recently, few studies had investigated the effects of the KD on the gut microbiome in health and disease[11],
60 but this has now changed, with a number of new studies published over the last three years[6,8]. These
61 studies remain largely descriptive regarding dietary-induced gut microbiome changes and the role of the
62 gut microbiome in maintaining the reported anti-cancer effects of the KD in the context of CRC has not
63 yet been investigated. Therefore, we set out to investigate the importance of the gut microbiome in the
64 context of KD consumption in CRC. We first generated a humanized gut microbiome mouse model of CRC,
65 through the transplantation of stool samples from five healthy human donors. We then combined this
66 model with a therapeutically administered KD and were able to confirm the cancer-suppressing properties

67 of the KD. Most importantly, we could demonstrate, for the very first time, the causal role of the gut
68 microbiome in maintaining this effect, through transplantation of the microbial community. We report
69 long-lasting alterations in gut microbiome function in the absence of maintained selective pressure by the
70 KD. In our experiments, fecal stearic acid levels were increased not only upon KD consumption, but also
71 upon cecal transplantation, suggesting that the shift in the microbial community contributes to the
72 changes in the fatty acid pool. Importantly, potential stearate-producing members were enriched in
73 ketogenic conditions, whereas consumers were depleted.
74

75 **Results**

76 **KD leads to reduced colonic tumor burden and inflammatory response in CRC**

77 To study the relevance of the gut microbiome in CRC development in a model relevant to human
78 disease, we first established a representative healthy human microbiome by mixing fecal samples from
79 five healthy donors (5HD; Extended Data Fig. 1a for patient metadata). The achieved 5HD mix
80 recapitulated the compositions of the individual donor samples, as evidenced by family, genus and species
81 level analysis of whole genome shotgun sequencing (WGS, Extended Data Fig. 1b-d, respectively), while
82 fecal metabolite levels varied across samples (Extended Data Fig. 1e). We performed fecal microbial
83 transplantation (FMT) of the 5HD mix into germ-free (GF) and antibiotic-treated specific-pathogen-free
84 (SPF) mice in an AOM/DSS CRC model (Fig. 1a and 1b, details can be found in the methods section)
85 followed by a switch from standard to ketogenic diet after the last cycle of DSS. No significant difference
86 in body weight between the standard diet (SD) and ketogenic diet (KD) groups was observed throughout
87 the experiments, although dips in mouse body weight were observed following the antibiotic treatment
88 and following each cycle of DSS (Extended Data Fig. 2a and 2b). There was no difference in colon length
89 between groups (Extended Data Fig. 2c, GF). KD-fed mice exhibited a lower colonic tumor burden (Fig. 1c
90 (GF) and Fig. 1d (SPF)) and a smaller tumor size (Fig. 1e, 1f and 1g (SPF)) than SD-fed mice.

91 Characterization of full-length lamina propria (LP), mesenteric lymph node (MLN) and spleen
92 immune cell profiles (Extended Data Fig. 2d and 2e) showed a reduction in almost all LP $CD4^+$ T cell
93 populations in KD-fed mice. Only LP natural killer T cells and type 3 innate lymphoid cells (GF LP) were
94 increased – both have been associated to gut homeostasis and health[12]. Finally, the expression of both
95 subunits of calprotectin (a biomarker of inflammation used in inflammatory bowel disease[13]) was reduced
96 in the spleens of GF KD-fed mice (Fig. 1h and 1i). Nevertheless, it remains unclear whether the reduction
97 in immune cell populations reflects reduced inflammation induced by the KD or is rather a direct
98 consequence of the reduced tumor development.

99 To further assess the importance of KD in modulating inflammation in CRC, we employed a low-
100 grade inflammatory model, in which mice received four doses of AOM and were randomized into one of
101 three subgroups - GF, 5HD mix FMT, single CRC patient FMT, each with a KD and SD branch (Extended
102 Data Fig. 3a, 3b (5HD) and 3c (CRC)). A single CRC donor was used for colonization, rather than a mix of
103 multiple samples, due to the observed dissimilarities of microbial profiles between patients in our in-
104 house CRC stool collection. Despite the induction of ketosis in KD-fed mice (Extended Data Fig. 3d), we
105 observed no significant differences in colonic tumor burden between groups (Extended Data Fig. 3e), nor
106 in immune cell profiles (Extended Data Fig. 3f), suggesting not only that the KD specifically exerted its anti-
107 cancer effect in an inflammatory setting, independent of ketosis, likely by reducing inflammation, but also
108 that the fecal microbiome from this CRC patient did not exhibit a higher potential for CRC induction in this
109 setting, in contrast to observations made by Wong et al.[14]. Of note, long-term KD feeding induced fatty
110 liver and fibrosis in all sub-groups (Extended Data Fig. 3g), and as previously reported for long-term KD
111 consumption[15]. Altogether, these results suggest that the KD exerts an anti-tumorigenic effect in CRC,
112 potentially by modulating the immune system.

113

114

115 **KD induces a distinct host metabolic profile**

116 Ordination analyses based on the underlying β-diversity among host plasma samples collected
117 from animals undergoing ketogenic dietary intervention in the AOM/DSS inflammatory model of CRC,
118 revealed clustering based on dietary condition (Extended Data Fig. 4a (SPF) an Extended Data Fig. 4b (GF)).
119 β-HB plasma levels were elevated in KD-fed mice (Extended Data Fig. 4c (SPF) and 4d (GF)), confirming
120 ketosis. KD-fed mice presented altered amino acid, fatty acid, sugar, carbohydrate, vitamin, and bile acid
121 metabolism (Supp. Table 1 and Extended Data Fig. 4e (SPF), Supp. Table 2 and Supp Fig. 4f (GF).
122 Furthermore, mannose was increased in KD-fed mice (Supp. Table 1 (SPF) and 2(GF)). Interestingly,
123 mannose has been reported to possess antitumor properties[16], impairing tumor cell growth *in vitro* and
124 *in vivo*[17], and targeting tumor-associated macrophages[18]. While treatment with β-hydroxybutyrate
125 showed no effect, treatment with the ketone bodies acetone and sodium acetoacetate tended to reduce
126 the differentiation of naive T cells into Th17 cells (Extended Data Fig. 4g and 4h), which play an important
127 role in maintaining gut homeostasis[19] and are affected by KD in a dose-dependent manner[5]. Treatment
128 with a commercially available lipid mixture mimicking KD (containing arachidonic, linoleic, linolenic,
129 myristic, oleic, palmitic and stearic acid) led to a dose-dependent reduction in Th17 differentiation
130 (Extended Data Fig. 4i), as did treatment with some individual fatty acids, such as palmitic and oleic acid
131 (Extended Data Fig. 4j), suggesting that Th17 cells are susceptible to fatty acid modulation, but that
132 different fatty acids may exhibit different effects. Collectively, these data indicate that KD induces
133 systemic functional metabolic changes in the host, which are not limited to the induction of ketosis.

134

135 **The anti-cancer effects of the KD are mediated by the gut microbiome**

136 The gut microbiome may affect CRC development either by directly interacting with host cells
137 (attachment, invasion and translocation), or indirectly, through bacterial metabolism (genotoxins, SCFAs
138 and others)[20]. We first excluded bacterial translocation as a primary factor in the KD-mediated phenotype,

139 as mucus layer thickness (Extended Data Fig. 5a and 5b (GF)) and LPS levels in plasma (Extended Data Fig.
140 5c (GF) and 5d (SPF)) remained unaltered upon KD consumption, in line with Ang et al.[5]. To test the causal
141 role of the gut microbiome in our experimental setup, we performed a similar experiment in humanized
142 gut microbiome GF mice, however we housed the mice in open-top cages in a gnotobiotic flexible-film
143 isolator to allow for microbial exchange between groups (Extended Data Fig. 5e, 5f and 5g). Despite
144 confirmed ketosis, no difference in colonic tumor burden (Extended Data Fig. 5h), nor in colonic tumor
145 size (Extended Data Fig. 5i and 5j) was observed between groups. Furthermore, fecal microbial
146 compositions were similar in both groups (Extended Data Fig. 5k), with only a few taxa differentially
147 abundant between groups (Extended Data Fig. 5l), suggesting that microbial exchange between mice on
148 KD and SD was sufficient to negate the beneficial effects of the KD. Most importantly, we next performed
149 cecal microbial transplantation (CMT) of samples collected from the SPF diet mice (Fig. 1d) into a next
150 generation of SD-fed GF mice undergoing the same cancer model (Fig. 2a, Extended Data Fig. 5m).
151 Strikingly, KD-CMT mice, exhibited a lower colonic tumor burden than SD-CMT mice (Fig. 2b). Average
152 colonic tumor size per mouse did not differ between groups (Fig. 2c), however, KD-CMT mice exhibited a
153 smaller proportion of large tumors (Fig. 2d and e). Altogether, our results demonstrate the causal role of
154 the gut microbiome in mediating the previously observed KD-driven anticancer effect.
155
156 **KD induces a distinct fecal microbial profile**
157 Ordination analyses based on the underlying β-diversity among fecal samples collected from KD-
158 and SD-fed AOM/DSS mice revealed clustering of 5HD mix used for FMT with the individual healthy donor
159 stool samples and with the murine stool samples collected three days after FMT (TG, Fig. 3a (SPF) and 3d
160 (GF)), confirming the validity of the 5HD mix used for transplant and its engraftment. Furthermore, we
161 observed increasing differences between KD and SD samples over time (Fig. 3b (SPF) and 3e (GF)). Early
162 time points cluster together (T0, collected at diet change), while later time points diverge (T1-T4).

163 Differential analysis revealed *Akkermansia* spp., bacteria which can suppress colorectal tumorigenesis
164 through modulation of the immune system[21], *Intestimonas* spp., *Lachnoclostridium* spp., *Bilophila* spp.
165 (Fig. 3c (SPF)), *Phocea* spp., *Faecalitalea* spp. and others (Fig. 3f (GF), Supp. Table 3 (SPF) and 4 (GF)) to be
166 more abundant in KD, while *Bifidobacterium* spp., *Turicibacter* spp. (SPF), *Barnesiella* spp., *Eisenbergiella*
167 spp., *Ruminococcus 1* and *2* spp. (GF) and others were depleted. Furthermore, the differential abundance
168 of various members of *Barnesiellaceae* spp., *Erysipelotrichaceae* spp., *Lachnospiraceae* spp. and
169 *Ruminococcaceae* spp. suggested that dietary composition affects bacterial members of the same families
170 in different manners.

171 Investigation of the engrafted gut microbial communities at experimental endpoint revealed
172 distinct KD- and SD-associated microbiomes (Fig. 3g and 3h, Extended Data Fig. 6a, 6b (GF), 6c and 6d), as
173 well as KD-CMT- and SD-CMT-associated microbiomes (Fig. 3g and 3h, Extended Data Fig. 6c and 6d).
174 Although a selective pressure of the KD was observed, gut microbial composition differed between cecal
175 donor and recipient mice, likely due to the absence of continued selective pressure from the KD, or loss
176 of more fragile and hard-to-engraft bacteria (Fig. 3g). Metagenome-assembled genomes (MAGs),
177 representing abundant members of the microbial community, allowed us to achieve species-level
178 resolution. Noteworthy, some MAGs annotated as CRC-associated bacteria, such as *Rikenellaceae* spp.
179 (light blue) and *Muribaculaceae* spp. (dark blue, Fig. 3i, Extended Data Fig. 6e (GF)), were detected in SD
180 groups but not the KD groups. Interestingly, various *Alistipes* spp. were differentially abundant in all
181 experiments. Two MAGs (*Alistipes* and *COE* species) were only identified in KD-CMT, while 12 MAGs were
182 only identified in SD-CMT, among which *CAG-873*, *CAG-48* and *Parabacteroides distasonis* (Fig. 3i), also
183 identified in the donor SPF dietary experiment.

184

185

186

187 **Distinct fecal microbial functional profiles are maintained upon FMT**

188 As microbiome-mediated effects are based on the functional and metabolic capacities of different
189 microbes, we also investigated KD-induced functional changes. β-diversity analysis based on KEGG and
190 Pfam ordinations of SPF fecal samples revealed a clear separation between groups (Fig. 4a (KEGG) and
191 Extended Data Fig. 7a (Pfam)), suggesting selective pressure of the diet on the intestinal microbiota. This
192 could also be observed in the CMT experiment, where KD-CMT clustered separately from SD-CMT, despite
193 being maintained on SD (Fig. 4b (KEGG) and Extended Data Fig. 7d (Pfam)). Both SPF KD-fed and KD-CMT
194 mice exhibited a higher number of less abundant genes/Pfams than more abundant genes/Pfams,
195 suggesting a KD-induced functional depletion (Extended Data Fig. 7c (SPF, KEGG), 7d (CMT, KEGG), 7e
196 (CMT, KEGG) and 7f (CMT, Pfam)). Accordingly, gene set enrichment analysis (Fig. 3c) and
197 overrepresentation analysis (Extended Data Fig. 7g) of identified KEGG orthologs revealed differences in
198 carbohydrate metabolism between the treatment groups in the SPF diet and CMT experiments, such as
199 reduced starch and sucrose metabolism under ketogenic conditions. In line with this, genes assigned to
200 Pfams associated with carbohydrate metabolism accounted for a large proportion of over- and under-
201 represented genes under ketogenic conditions (Extended Data Fig. 7i (SPF) and Extended Data Fig. 7j
202 (CMT)). Furthermore, we found differential abundance of several CAZymes between dietary conditions,
203 which are known to play a crucial role in the building and breaking down of complex carbohydrates for
204 use by the organism[22], with an overall increase in glycosyltransferases (GT; Extended Data Fig. 7k).
205 Altogether, this data underlines the selective pressure of the KD on the gut microbiome, and its capacity
206 to shape long-term overall gut microbial function.

207

208

209

210 **The microbial metabolite stearate is elevated in ketogenic conditions and exhibits anticancer**
211 **effects**

212 In order to investigate the link between functional alterations of the gut microbiome and the
213 observed cancer phenotype, we investigated fecal metabolic profiles. Analysis of fecal metabolites
214 revealed distinct clustering of samples by condition in both the SPF dietary and CMT experiments (Fig. 4d
215 and 4e, respectively). Mice in the ketogenic conditions presented altered amino acid, fatty acid,
216 carbohydrate and SCFA profiles (Supp. Tables 5 and 6), albeit to a lesser extent in the CMT experiment. A
217 single detected long-chain fatty acid, namely octadecanoic acid (also known as stearic acid), was elevated
218 in KD (Fig. 4f) and KD-CMT (Fig. 4g) mice. Strikingly, stearic acid levels correlated with colonic tumor
219 burden in the SPF dietary experiment (Fig. 4h), with a similar trend observed in the CMT experiment,
220 suggesting a functional relevance of long-chain fatty acid metabolism in CRC. In addition, associations
221 between the abundances of all identified KEGG orthologs and tumor counts in the SPF dietary experiment
222 identified a correlation between colonic tumor burden and some lipid-metabolism-associated KEGGs,
223 such as FabH, 3-oxoacyl-[acyl-carrier-protein] synthase III (K00648), FabB, 3-oxoacyl-[acyl-carrier-protein]
224 synthase I (K00647), FabZ, 3-hydroxyacyl-[acyl-carrier-protein] dehydratase (K02372), and FabF, 3-
225 oxoacyl-[acyl-carrier-protein] synthase II (K09458) (Fig. 5a and 5b, Extended Data Fig. 8a). Indeed, core
226 fatty acid biosynthesis KOs were less abundant in the ketogenic diet group of the SPF diet experiment,
227 except for the different enoyl-carrier ACPs and the thioesterases, of which one or more can be found in
228 most bacterial genomes (Fig. 5c). Reflecting their essential function, the core enzymes of the fatty acid
229 synthesis pathway correlating with tumor counts were found in both Bacteroidetes and Firmicutes
230 genomes. In KD, contigs carrying K00647, K00648, K09458 and K02372 were assigned to *Akkermansia*
231 spp., *Flavonifractor* spp. and uncharacterized Firmicutes genera, whereas many SD contigs were assigned
232 to Bacteroidetes genera (*Bacteroides* spp., *Parabacteroides* spp., *Muribaculum* spp. and uncharacterized
233 Bacteroidetes; Extended Data Fig. 8b).

234 Given that different bacterial taxa are known to produce and consume different fatty acids, which
235 are used for membrane biogenesis and as signaling molecules, we further investigated which bacterial
236 taxa may be responsible for the release of fatty acids, including stearic acid, and which bacteria may be
237 able to uptake free fatty acids. Interestingly, detection of long-chain fatty acids in different bacterial
238 cultures (Fig. 6a and 6b; re-analysis of the publicly available dataset from the Sonnenburg lab[23]), revealed
239 that – in line with the shifts in the microbial communities observed under KD (Fig. 6c and Extended Data
240 Fig. 8c) - the *Ruminococcaceae* and *Lachnospiraceae* families, both belonging to the class Clostridia, were
241 consistent producers of stearic acid, while *Tanerellaceae* and *Bacteroidaceae,* both belonging to the class
242 Bacteroidia, were consistent consumers (Fig. 6a). The *Clostridiaceae* family was composed of both
243 producers and consumers of stearic acid (Fig. 6a). The observed contrast between the abundance of fatty
244 acid release KOs and actual production/consumption of stearic acid by different bacteria as detected in
245 the Sonnenburg dataset suggests that different bacteria contribute differently to the overall fatty acid
246 pool. Therefore, despite no difference in the overall abundance of K10804 and K07030 between dietary
247 conditions (Fig. 5c), when assigned to stearate-producing bacterial families (as detected in the
248 Sonnenburg dataset), these KOs may result in increased levels of stearate, as we observed in ketogenic
249 conditions, while when assigned to stearate-consuming families, they may result in a decrease in stearate
250 levels, as we observed in standard conditions. Importantly, acyl-CoA thioesterase I TesA (K10804), a key
251 thioesterase responsible for the release of fatty acids from their acyl carrier, alongside the fatty acid kinase
252 FakA (K07030) used by Gram-positive bacteria to activate exogenous fatty acids, were inversely correlated
253 with colonic tumor burden in the SPF dietary experiment (Fig. 5d). A larger proportion of K10804 was
254 assigned to Clostridia in the ketogenic condition, and Bacteroidia in the standard condition in both
255 experiments (Fig. 5d), indicating that the lower levels of luminal stearate detected in standard conditions
256 may be due to the increased abundance of Bacteroidia, which, although they harbor the gene for fatty
257 acid release, are known stearate consumers[23]. K07030 was largely attributed to Clostridia and other

258 Firmicutes (Fig. 5d), suggesting that these bacteria can uptake exogenous fatty acids (for example from
259 the ketogenic diet) and might further elongate them into other long-chain fatty acids for downstream use
260 or release. To assess the putative anti-cancer properties of the long-chain fatty acid of interest identified
261 in the dietary and CMT experiments, we treated various CRC cell lines with increasing concentrations of
262 stearic acid. We observed a dose-dependent reduction in cell growth (Fig. 6d, 6e, 6f, Extended Data Fig.
263 8d, 8e, 8f), highlighting stearic acid as an anti-cancer metabolite. Furthermore, this observation was
264 specific to elevated levels of stearic acid, as treatment with other long-chain fatty acids did not exhibit
265 anti-cancer properties, even at higher concentrations (Fig. 6g and Extended Data Fig. 8g).

266 Altogether, these results suggest that KD consumption can lead to lasting functional effects on
267 the gut microbiome, affecting the bacterial secretome, and persisting even when the selective pressure
268 of the KD itself is no longer present.

269

270 **Discussion**

271 In this study we identified the gut microbiome as a driving factor in the anti-cancer effect of KD in
272 CRC. We observed that KD alters gut microbial function, namely bacterial carbohydrate metabolism and
273 the fatty acid pool. Upon KD consumption and following microbial transplantation, we observed an
274 increase in fecal octadecanoic acid, a long-chain fatty-acid, which exhibited anti-cancer properties *in vitro*.

275 The anticancer properties of the ketone body β-HB have been reported in several instances[3,4],
276 however, despite confirmed induction of ketosis in these mice, we observed the absence of a KD-induced
277 anticancer effect in the absence of robust gut microbial changes. Thus, ketosis alone seems to be
278 insufficient to ensure CRC suppression, similarly to other studies showing no KD benefits in the context of
279 cancer, despite the induction of ketosis[3,24].

280 Our results instead suggest that the anti-cancer effect of KD is based on gut microbial function,
281 rather than composition. The importance of microbial function rather than microbial composition of the

282 intestinal flora can be observed in other contexts as well. In melanoma, three different studies
283 demonstrated that the microbiome was responsible for ensuring the response to checkpoint inhibitor
284 therapy[25–27]. Interestingly however, these studies highlighted distinct bacterial species underlying this
285 response, suggesting that microbiome-encoded functions rather than individual bacterial species are
286 important in driving therapy response.

287 In regard to our own study, the depletion of dietary carbohydrates is known to provide a growth
288 advantage for certain bacteria, such as *Alistipes* spp., *Bilophila* spp. and mucin-degraders like *Akkermanisa*
289 spp., whereas *Bifidobacterium* spp. and some *Bacteroides* spp. are typically depleted[5,28], most likely due
290 to their preference for dietary carbohydrates over host glycans[29–31]. The shift from taxa dependent on
291 dietary carbohydrates taxa to taxa able to use alternative energy sources is reflected in the CAZyme profile
292 shift in KD and KD-CMT mice. For instance, the glycosylhydrolase GH101, enriched in all three of our
293 metagenomic datasets, is mucin-specific, and is required to cleave core-1 *O*-linked glycans[32]. In contrast,
294 the glycosylhydrolases GH50, present in the genomes of many *Bacteroides* spp. and *Proteobacteria* spp.,
295 and GH128, amongst others present in the genomes of the strongly reduced *CAG-485* and *CAG-873*
296 members, are specific for dietary carbohydrates[33] and accordingly found in reduced abundance following
297 KD intervention. These specific effects clearly demonstrate how diet systematically shapes the taxonomic
298 composition of the microbiome, driven and accompanied by a functional adaptation of the microbiome
299 to the new environment.

300 Although still an ongoing debate, the link between mucin-degrading bacteria and gut barrier
301 function is well-described. While overgrowth of mucin-degrading bacteria are known to damage the
302 epithelium[34], microbial mucin metabolism is considered beneficial as it is known to change the
303 glycosylation profile of the intestine[35,36], and increase mucin turnover[37]. Indeed, no mucus thinning could
304 be observed in KD-fed mice.

305 Analysis of the fecal metabolomes in the dietary intervention and CMT experiments identified
306 differences in the fatty acid pool. Amongst others, microbiome-derived fatty acids have an
307 immunomodulatory potential[38,39]. Interestingly, both *A. muciniphila* and *R. gnavus* produced higher levels
308 of palmitic and stearic acid when grown in the presence of mucins, linking bacterial fatty acid metabolism
309 to mucin physiology. In addition to their essential role in membrane biogenesis, fatty acids produced by
310 bacteria have signaling functions and play an essential role in host-microbe interactions[38]. The fatty acid
311 profile is highly species-, or even strain-, and substrate-dependent and various microbial-derived fatty
312 acids have different effects linking bacterial fatty acid metabolism to host health and disease[38].

313 Stearic acid, a long-chain fatty-acid, can originate from the diet, the host[40] and the gut
314 microbiome[41]. Stearic acid is normally desaturated by the host enzyme SDC1[42], is downregulated upon
315 reduced glucose intake and has been linked to inflammation[43–45]. Recently, Kindt et al. showed that
316 microbiome-derived acetate activated SDC1 and promoted fatty acid desaturation[46]. Furthermore, certain
317 members of the gut microbiome can directly affect stearic acid levels by consuming it as an exogenous
318 fatty acid for membrane lipid synthesis[23], producing it *de novo*[47], transforming it from oleic acid, or as a
319 product of mono- and polyunsaturated acid degradation[48,49]. In our experiments, as fecal stearic acid
320 levels were increased not only upon KD consumption, but also in KD-CMT, it is likely that the shift in the
321 microbial community is contributing to the changes in the fatty acid pool. Importantly, potential stearate-
322 producing members were enriched by the KD, whereas consumers were depleted (Fig. 6a and 6c).

323 Furthermore, several studies investigating the properties of stearic acid have demonstrated its
324 anti-cancer effects, both *in vitro* and *in vivo*. Stearic acid inhibited colony formation in different human
325 cancer cell lines[50], reduced tumor burden in rat model of mammary carcinoma[51], possibly by inducing
326 apoptosis via signaling through protein kinase C[52]. Finally, a recent study was able to not only validate the
327 suppression of colorectal adenocarcinoma by stearic acid, but also its synergy with 5-FU treatment[53]. This

328 effect might not be limited to stearic acid and its implications for human health and CRC in particular need
329 further investigation.

330 Based on our observations in the context of this study, the gut microbiome plays a central role in
331 ensuring the anti-cancer effects of the KD in the context of a murine model of inflammation-driven CRC.
332 Nevertheless, within this experiment, we can observe a more pronounced anti-cancer phenotype for
333 some mice than for others. This might indicate that the initial gut microbiome profile may determine
334 whether an individual is a “responder” or a “non-responder” to the KD in the context of CRC. The concept
335 of “responders” and non-responders” has been explored, albeit to a relatively limited extent, in epilepsy
336 patients who undergo KD therapy for the reduction of seizures[54]. Furthermore, the response to some
337 cancer treatments, such as immune checkpoint inhibition depend on gut microbial composition[55], and
338 ketogenic dietary regimens may be able to enhance the effects of these therapies[8]. Future studies
339 identifying biomarkers to predict response to dietary intervention based on the resident gut microbiome
340 and studies aiming to transform a “non-responder” microbiome into a “responder” microbiome would be
341 a significant step forward towards personalized patient care.

342

343

344

345

346

347

348

349

350

351

352 **Figure legends**

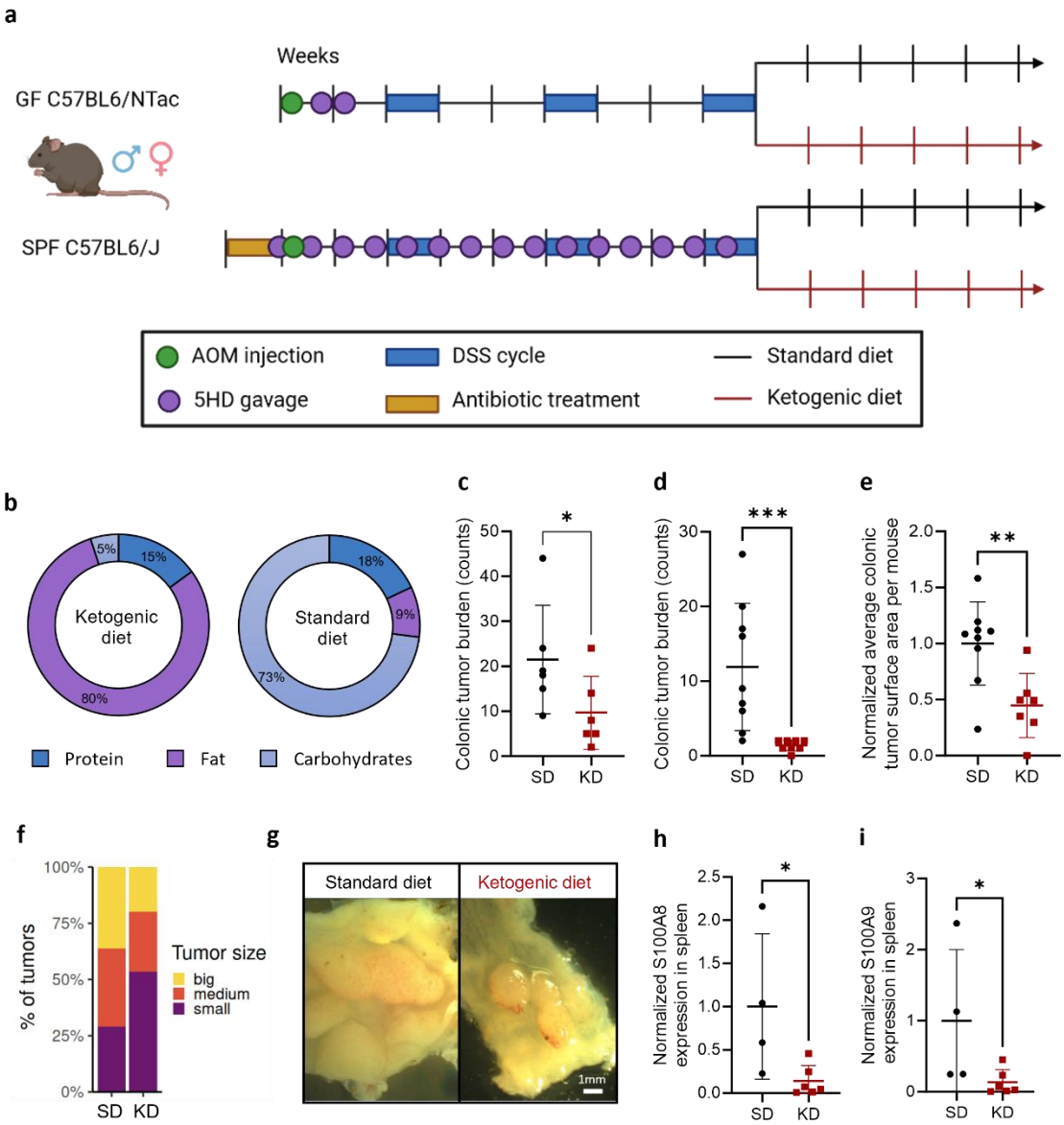

353

354 **Figure 1. Ketogenic diet leads to lower colonic tumor incidence and smaller tumor size in an**
355 **inflammatory model of CRC. | a.** Schematic representation of the dietary AOM/DSS experimental setup
356 in the GF (top) and SPF (bottom) facilities (created with BioRender.com). **b.** Compositions of the KD and
357 SD, with % of calories from the indicated source. **c.** Colonic tumor burden in GF KD- and SD-fed mice. **d-f.**
358 Colonic tumor burden (**d**), normalized average colonic tumor surface area per mouse (**e**) and tumor

surface area distribution (small= first tertile, medium=second tertile, big=third tertile; Chi-squared test $\chi 2$ (2, N = 87) = 3.4, p = 0.184; **f**) in SPF KD- and SD-fed mice. **g.** Representative images of the distal portion of the colon from one KD- and one SD-fed mouse in the SPF facility. Scale bar = 1mm. **h-i.** Normalized S100A8 (**f**) and S100A9 (**g**) expression in the spleens of mice from the GF diet experiment, as determined by qPCR. Data is shown as mean±SD in (**c**), (**d**), (**e**), (**h**), and (**i**). Data in (**c**) shows n=6 mice per condition from one experiment. Data in (**d**), (**e**) and (**f**) shows n=8 and 9 mice in the KD-fed condition and the SD-fed conditions respectively, pooled from two independent experiments in the SPF facility. Data in (**f**) and (**g**) shows n=4 mice per condition from one experiment in the GF facility. Two-tailed Mann-Whitney U test in (**c**), (**d**), (**e**), (**h**), and (**i**), * p<0.05, ** p<0.01, *** p<0.001.

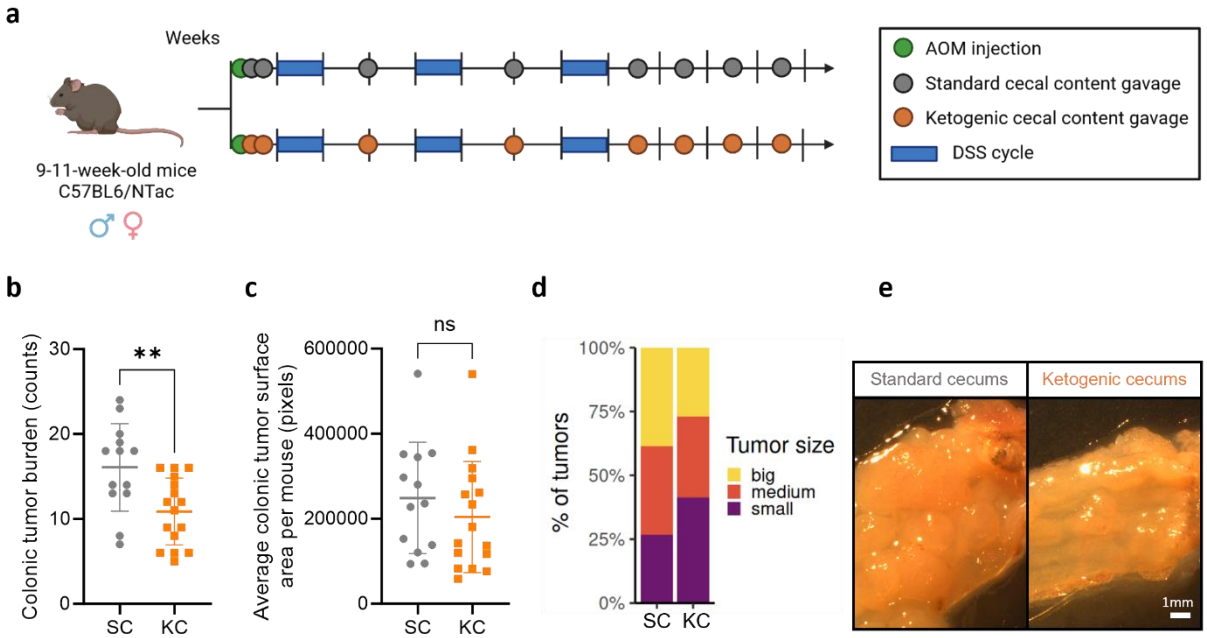

Figure 2. The tumor-inhibitory effect of ketogenic diet is mediated by the gut microbiome. | a. Schematic representation of the cecal microbial transfer experimental setup in the GF facility (created with BioRender.com). **b-e.** Colonic tumor burden (**b**), average colonic tumor surface area per mouse (in pixels) (**c**), and tumor surface area distribution (small= first tertile, medium=second tertile, big=third

373 tertile; Chi-squared test $\chi 2$ (2, N = 384) = 10.3, p = 0.00586; **d**), in KC and SC recipient mice. n=16 KC
374 recipient mice and n=13 SC recipient mice. Cecal matter from n=8 different donor mice per condition was
375 used for CMT. Data shown as mean±SD in (**b**) and (**c**). Two-tailed Mann Whitney U test, **p<0.01,
376 ***p<0.001 in (**b**) and (**c**). **e.** Representative images of the distal portion of the colon from one KC and SC
377 recipient mouse. Scale bar = 1mm.

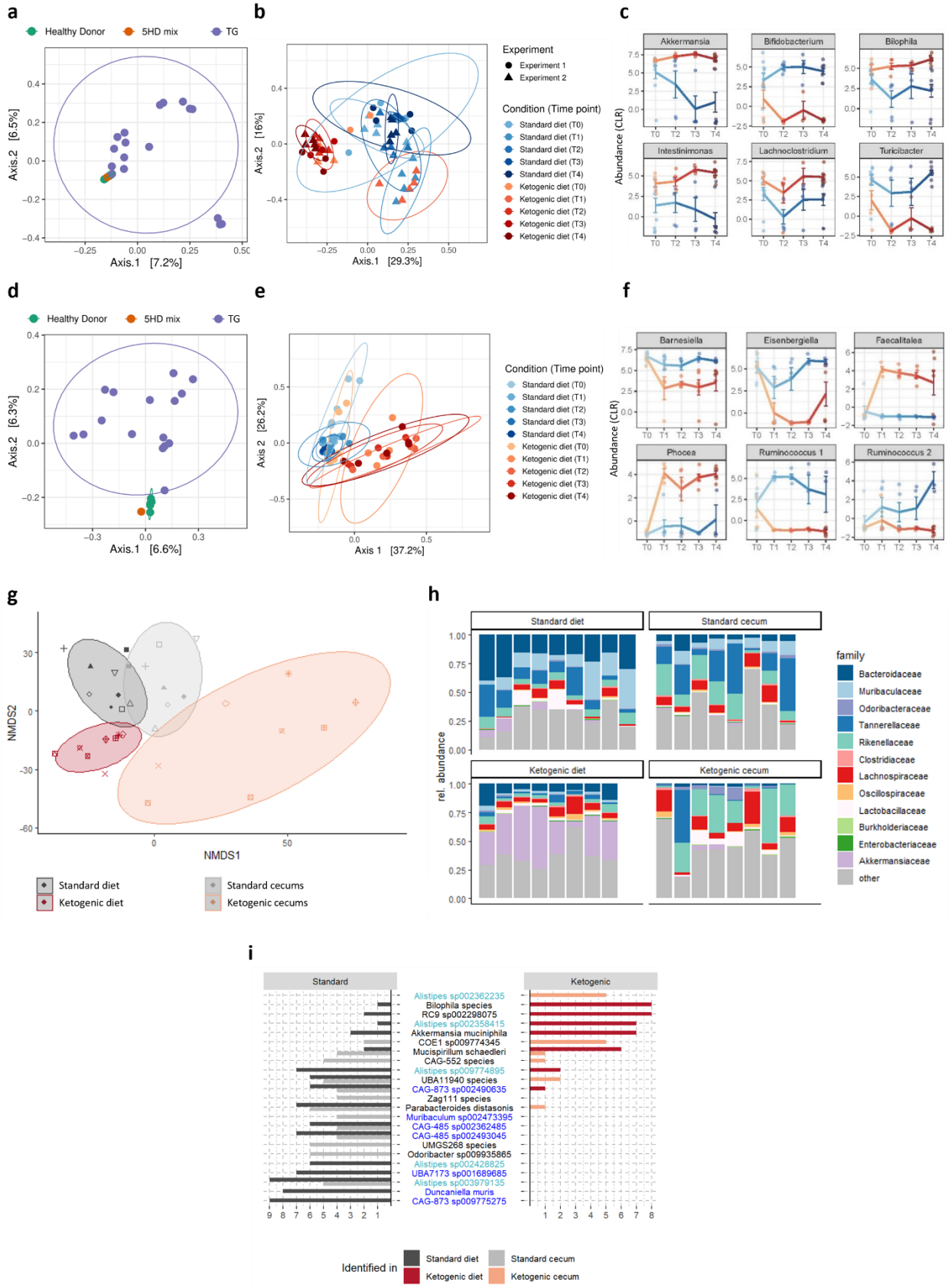
a
Healthy Donor
5HD mix
TG
Axis.2 [6.5%]
Axis.1 [7.2%]
b
Axis.2 [16%]
Axis.1 [29.3%]
Experiment
Experiment 1
Experiment 2
Condition (Time point)
Standard diet (T0)
Standard diet (T1)
Standard diet (T2)
Standard diet (T3)
Standard diet (T4)
Ketogenic diet (T0)
Ketogenic diet (T1)
Ketogenic diet (T2)
Ketogenic diet (T3)
Ketogenic diet (T4)
c
Akkermansia
Bifidobacterium
Bilophila
Intestinimonas
Lachnoclostridium
Turicibacter
Abundance (CLR)
d
Healthy Donor
5HD mix
TG
Axis.2 [6.3%]
Axis.1 [6.6%]
e
Axis 2 [26.2%]
Axis 1 [37.2%]
Condition (Time point)
Standard diet (T0)
Standard diet (T1)
Standard diet (T2)
Standard diet (T3)
Standard diet (T4)
Ketogenic diet (T0)
Ketogenic diet (T1)
Ketogenic diet (T2)
Ketogenic diet (T3)
Ketogenic diet (T4)
f
Barnesiella
Eisenbergiella
Faecalitalea
Phocea
Ruminococcus 1
Ruminococcus 2
Abundance (CLR)
g
NMDS2
NMDS1
Standard diet
Ketogenic diet
Standard cecums
Ketogenic cecums
h
Standard diet
Standard cecum
Ketogenic diet
Ketogenic cecum
rel. abundance
family
Bacteroidaceae
Muribaculaceae
Odoribacteraceae
Tannerellaceae
Rikenellaceae
Clostridiaceae
Lachnospiraceae
Oscillospiraceae
Lactobacillaceae
Burkholderiaceae
Enterobacteriaceae
Akkermansiaceae
other
i
Standard
Ketogenic
Alistipes sp002362235
Bilophila species
RC9 sp002298075
Alistipes sp002358415
Akkermansia muciniphila
COE1 sp009774345
Mucispirillum schaedleri
CAG-552 species
Alistipes sp009774895
UBA11940 species
CAG-873 sp002490635
Zag111 species
Parabacteroides distasonis
Muribaculum sp002473395
CAG-485 sp002362485
CAG-485 sp002493045
UMGS268 species
Odoribacter sp009935865
Alistipes sp002428825
UBA7173 sp001689685
Alistipes sp003979135
Duncaniella muris
CAG-873 sp009775275
Identified in
Standard diet
Standard cecum
Ketogenic diet
Ketogenic cecum

378

379 **Figure 3. Ketogenic diet alters gut microbiome composition. | a-f.** β-diversity as assessed by PCoA (95%
380 confidence interval) of Bray-Curtis distance in five individual healthy donor stool samples, in a mix of the
381 five healthy donor stool samples (5HD mix) and in murine fecal samples three days after gavage (TG, **a**
382 and **d**); β-diversity as assessed by PCoA (95% confidence interval) of Bray-Curtis distance in murine fecal
383 samples collected over time after diet change (**b** and **e**); Abundance of selected genera which are
384 differentially abundant at at least one time point (using a generalized linear model on CLR, **c** and **f**) in fecal
385 samples collected over time after diet change from SD- and KD-fed mice in the SPF (**a**, **b** and **c**) and GF (**d**,
386 **e**, and **f**) dietary experiments (T0 at diet change, T1-T4 weeks after diet change), as analyzed by 16s rRNA
387 sequencing. **g-i.** β-diversity as assessed by NMDS (95% confidence interval) of Euclidean distance (**g**),
388 relative abundance of bacterial families (**h**), and highly characteristic bacterial MAGs (detected in at least
389 six mice in one condition but not more than three mice in the other (diet experiment); detected in at least
390 four mice in one condition but not more than three mice in the other (CMT experiment), **i**) detected in
391 KD, SD, KC and SC murine fecal samples at endpoint, as analyzed by WGS. In (**i**), *Rikenellaceae* are
392 highlighted in light blue and *Muribaculaceae* in dark blue. Data shows results from n=8 SPF KD-fed mice,
393 n=9 SPF SD-fed mice, pooled from two independent experiments in (**a**), (**b**), (**c**), (**g**), (**h**) and (**i**) ; n=3 GF SD
394 and n=6 GF KD mice from one experiment in (**d**), (**e**), (**f**) and n=8 KC and n=8 SC mice from one experiment
395 in (**g**), (**h**) and (**i**).

396

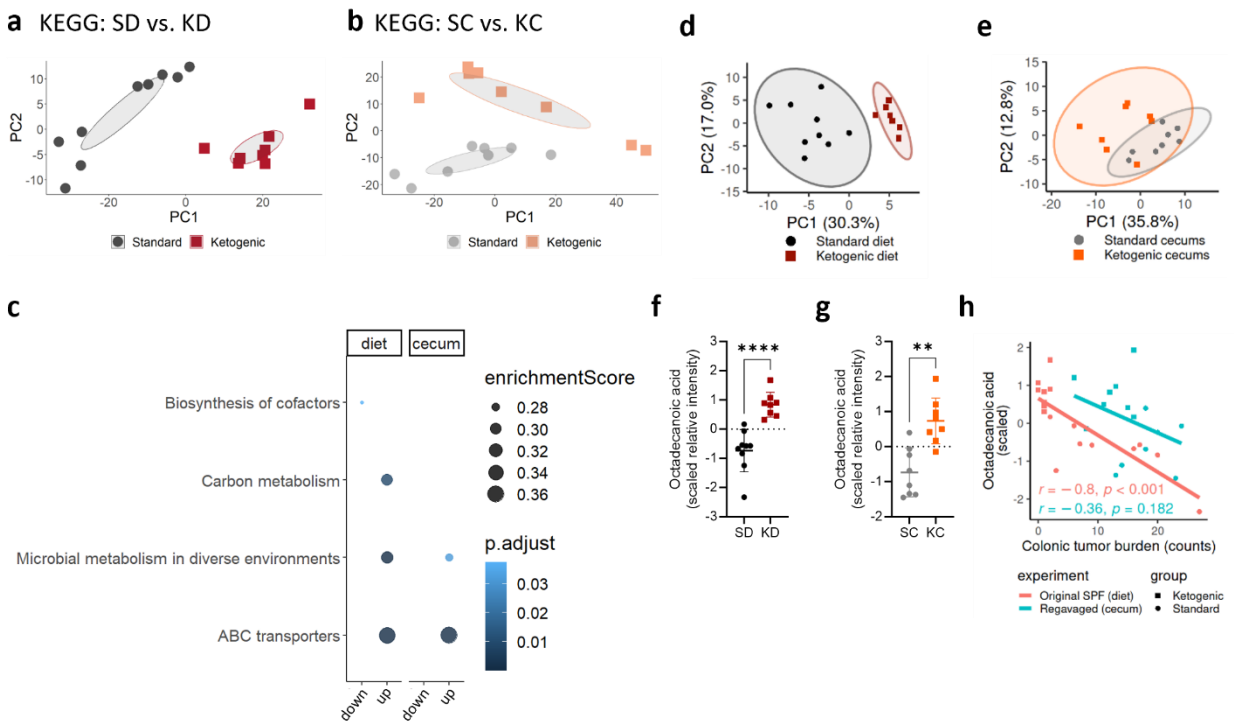

Figure 4. Ketogenic diet alters gut microbial function and metabolic profiles, leading to elevated levels of fecal stearate. | a-b. PCA (95% confidence interval) of the predicted functional features of the gut microbiome (KEGG) of SPF KD- and SD-fed mice at endpoint. **c.** Gene set enrichment analysis (GSEA, KEGG) of differentially abundant genes (threshold p.adj. < 0.05) between KD, SD, KC and SC fecal samples at endpoint. **d-e.** PCA (95% confidence interval) of identified metabolites from fecal samples from SPF KD- and SD-fed mice (**d**) and from KC and SC recipient mice (**e**), as analyzed by united GC-MS and LC-MS. **f-g.** Scaled octadecanoic acid (stearic acid) levels detected in fecal samples from SPF KD- and SD-fed mice (**f**) and from KC and SC recipient mice (**g**), as detected by LC-MS. **h.** Correlation of colonic tumor burden with fecal octadecanoic acid levels in SPF KD- and SD-fed mice (red) and in KC and SC recipient mice (blue). Two-sided Pearson correlation testing was used. Data shown in (**a**), (**c**), (**d**), (**f**) and (**h, red**) are from n=9 SPF SD-fed and n=8 SPF KD-fed mice, pooled from two independent experiments. Data shown in (**b**), (**c**), (**e**), (**g**) and (**h, blue**) are from n=8 mice per condition. Two-sided Mann-Whitney test in (**f**) and (**g**); ns $p > 0.05$, * $p \leq 0.05$, ** $p \leq 0.01$, *** $p \leq 0.001$, **** $p \leq 0.0001$.

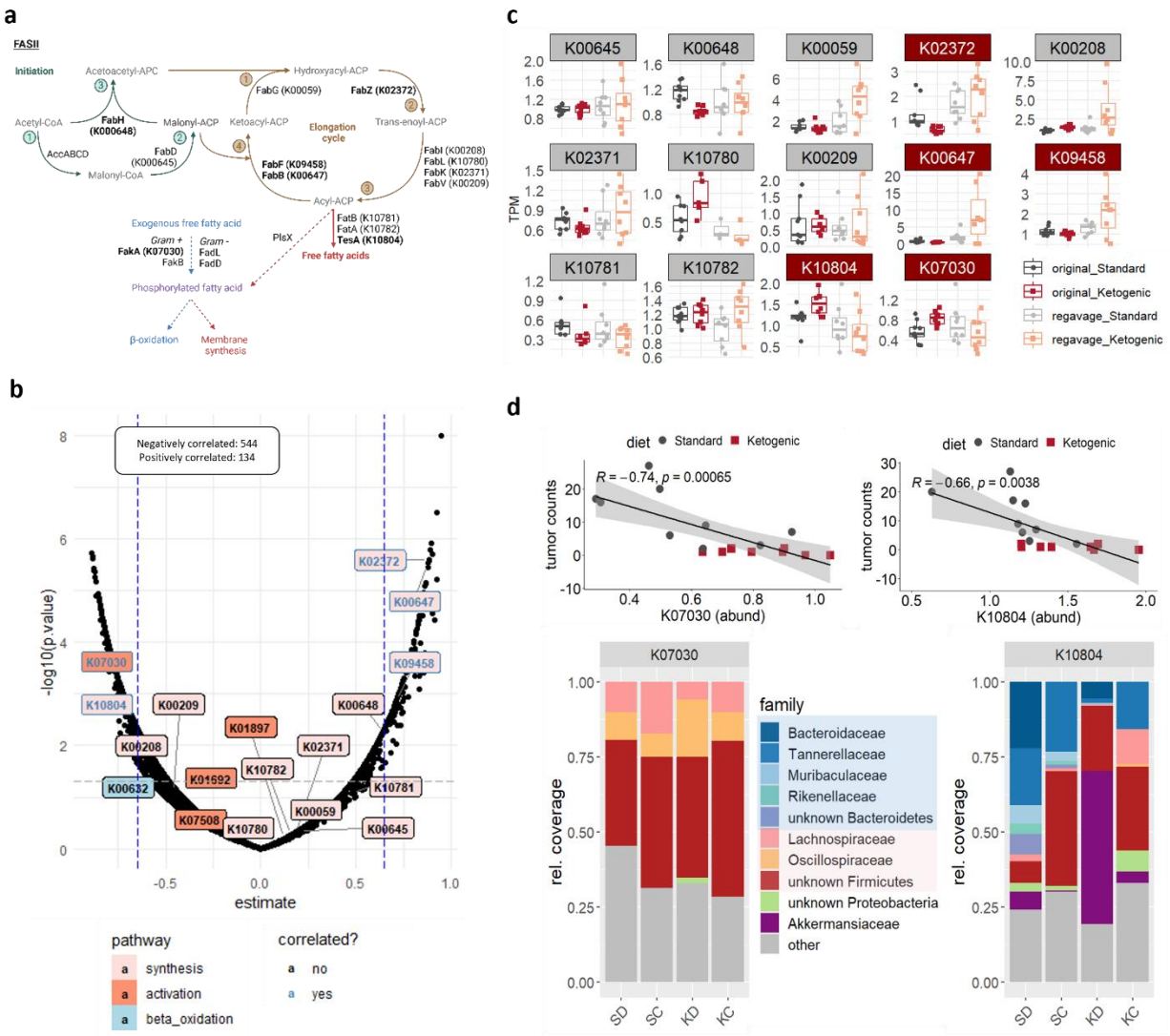

Figure 5. Stearate is a microbial metabolite. |a. Schematic representation of type II bacterial fatty acid synthesis created with BioRender, adapted from Yao et Rock (2017)[41]. Core enzymes are shown with their corresponding KOs. The abundance of bolded KOs correlates with colonic tumor burden in KD- and SD-fed mice. Abbreviations: acetyl-CoA carboxylase enzyme complex (AccABCD), β-ketoacyl-ACP synthase 1 (FabB), malonyl-CoA:ACP transacylase (FabD), β-ketoacyl-ACP synthase II (FabF), β-ketoacyl-ACP reductase (FabG), β-ketoacyl-ACP synthase III (FabH), enoyl-ACP reductase enzyme isoforms (FabI, FabK, FabL and FabV), β-hydroxyacyl-ACP dehydratase (FabZ), long-chain-fatty-acid-CoA ligase (FadD), long-chain fatty acid transport protein (FadL), fatty acid kinase (FakA, FakB), acyl-ACP thioesterase (FatA), iron

420 transport protein (FatB), thioesterase 1/protease 1/lysophospholipase L1 (TesA), phosphate
421 acyltransferase (PlsX), CoenzymeA (CoA), acyl carrier protein (ACP). **b.** Correlation analysis (Pearson)
422 between KO abundance and colonic tumor burden in KD- and SD-fed mice. Vertical blue dotted lines
423 represent thresholds for correlation coefficients (r) above and below 0.65 and -0.65, respectively. The
424 horizontal gray dotted line represents the threshold for statistical significance -log10(0.05). KOs involved
425 in fatty acid metabolism appear labelled on the volcano plot and are represented in different colors
426 (pink=synthesis, orange=activation and blue=β-oxidation). Of those, significantly correlated KOs are
427 labelled in light blue font. **c.** Abundance of selected KOs of interest (summed transcripts per million (TPM))
428 in fecal samples from KD- and SD-fed mice, and KC and SC recipient mice, at endpoint. The abundance of
429 KOs highlighted in red correlates with colonic tumor burden in KD- and SD-fed mice. **d.** Correlation
430 (Pearson) between colonic tumor burden and the selected KOs of interest K07030 and K10804 (**top**);
431 Relative taxonomic assignment of contigs encoding for the selected KOs of interest K07030 and K10804
432 at family level (**bottom**) detected in murine fecal samples from KD-, SD-fed, KC and SC recipient mice at
433 endpoint. Members of the class Bacteroidia are shaded in blue, while members of the class Clostridia are
434 shaded in red. . Data shown in (**b**), (**c, read and black**) and (**d**) are from n=9 SPF SD-fed and n=8 SPF KD-
435 fed mice, pooled from two independent experiments. Data shown in (**c, gray and orange**) are from n=8
436 mice per condition.

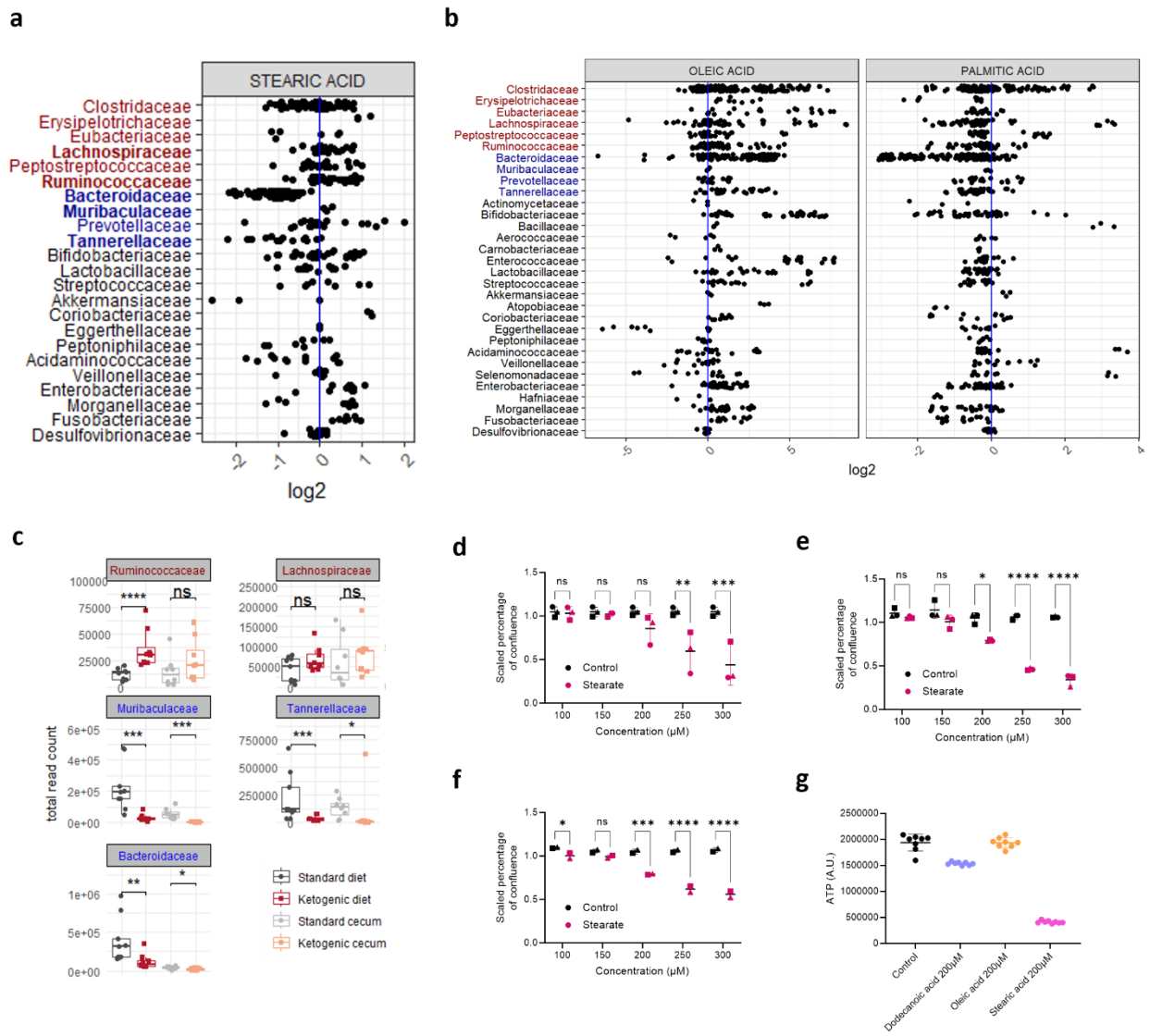

437

438 **Figure 6. The microbial metabolite stearate exhibits anticancer effects. | a-b.** Levels of stearic acid (**a**),

439 and oleic (**b, left**) and palmitic acid (**b, right**) measured in bacterial cultures (in relation to sterile growth

440 medium, shown as $\log_2$) of the Sonnenburg dataset. Members of the class Clostridia are listed in red, while

441 members of the class Bacteroidia are listed in blue. Total read counts detected in murine fecal samples

442 from KD-, SD-fed, KC and SC recipient mice at endpoint of members listed in bolded text are shown in (**c**).

443 **c.** Relative abundance (total read counts) of stearate-producing and -consuming families of interest

444 detected in murine fecal samples from KD-, SD-fed, KC and SC recipient mice at endpoint selected from

445 (**a**). **d-f.** Scaled HCT 116 (**d**), HT29 (**e**) and Caco2 (**f**) confluence at 72 hours after treatment with stearic
446 acid or corresponding controls (100µM, 150 µM, 200 µM, 250 µM, 300 µM). Data shows n=3 (for HCT116
447 and HT29) and n=2 (for Caco2) independent experiments (indicated by different datapoint shapes), each
448 with eight technical replicates per condition. **g.** ATP measurement (CellTiterGlo) of HT29 cells at 72 hours
449 after treatment with stearic acid, oleic acid, dodecanoic acid or control (200 µM). Data shows n=8
450 technical replicates from one experiment. Two-way ANOVA with multiple comparisons in (**c**), (**d**), (**e**) and
451 (**f**); **p<0.01, ***p<0.001. Data shown in (**c, red and black**) are from n=9 SPF SD-fed and n=8 SPF KD-fed
452 mice, pooled from two independent experiments. Data shown in (**c, gray and orange**) are from n=8 mice
453 per condition.

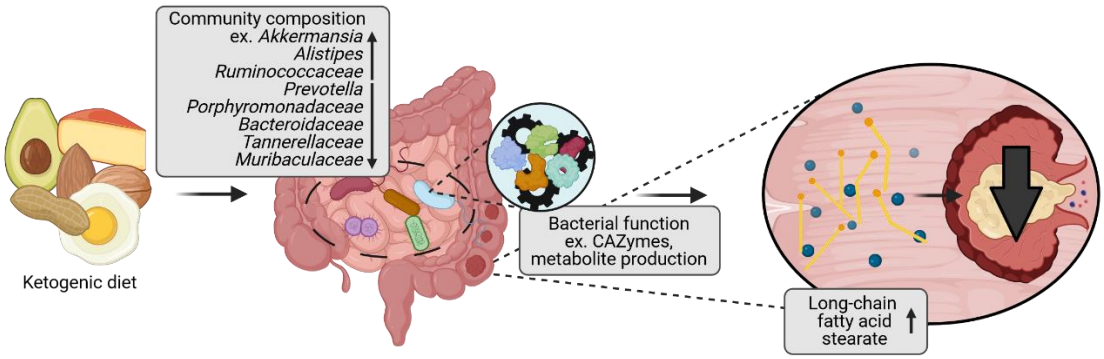

454

455 **Figure 7. Functional ketogenic-diet-induced changes in the gut microbiome are responsible for its anti-**
456 **cancer properties.**

457 Ketogenic diet consumption leads to lasting functional changes in the gut microbiome, such as alterations
458 in bacterial energy metabolism and in the long-chain fatty acid pool. The altered gut microbiome is
459 sufficient to reduce CRC development.

a

Donor number	1	2	3	4	5	6
Condition	Healthy	Healthy	Healthy	Healthy	Healthy	CRC
Gender	F	F	M	F	M	F
Age (years)	60	62	43	58	57	56
Cancer grade	N/A	N/A	N/A	N/A	N/A	G2

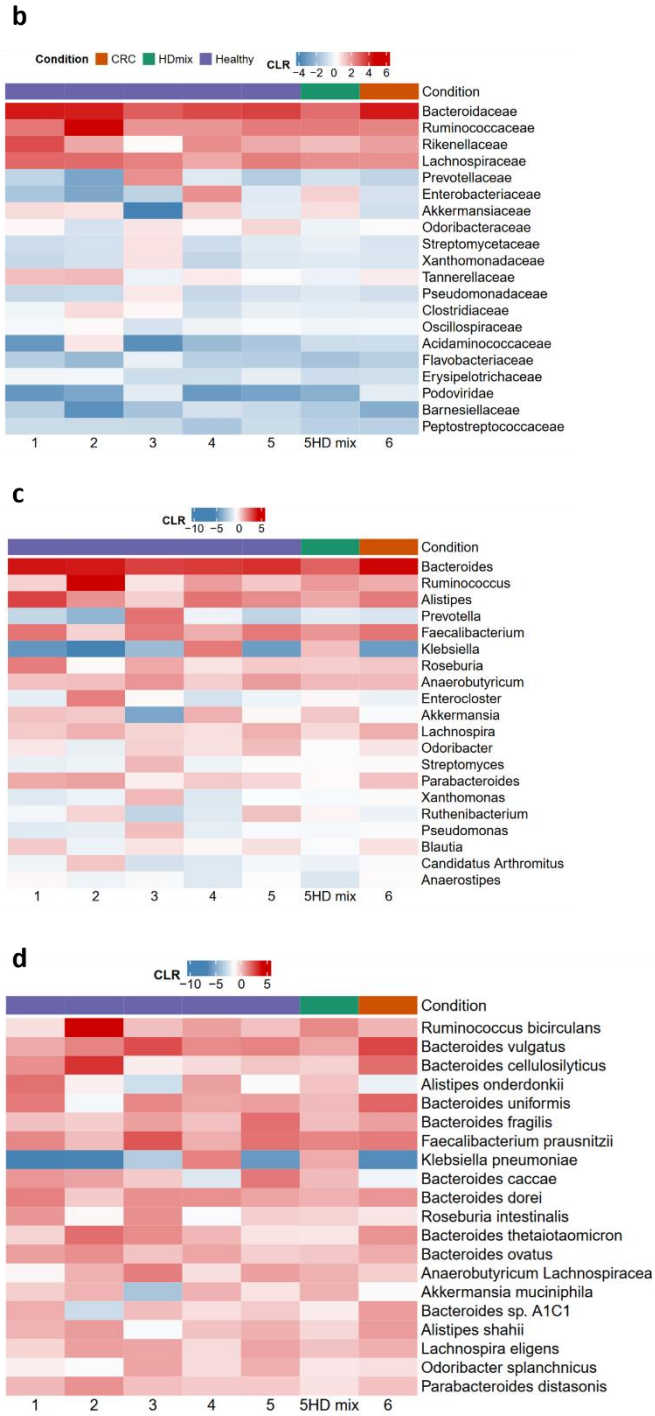

Extended data figure 1. | a. Metadata of fecal sample donors. M=male, F=female, N/A=not applicable, UNKN=unknown. **b-d.** Relative abundance of the top 20 most abundant bacterial families (**b**), genera (**c**)

463 and species (**d**) in human stool samples (CLR units)**. e.** Relative metabolite levels detected in human fecal

464 samples, analyzed by untargeted LC-MS.

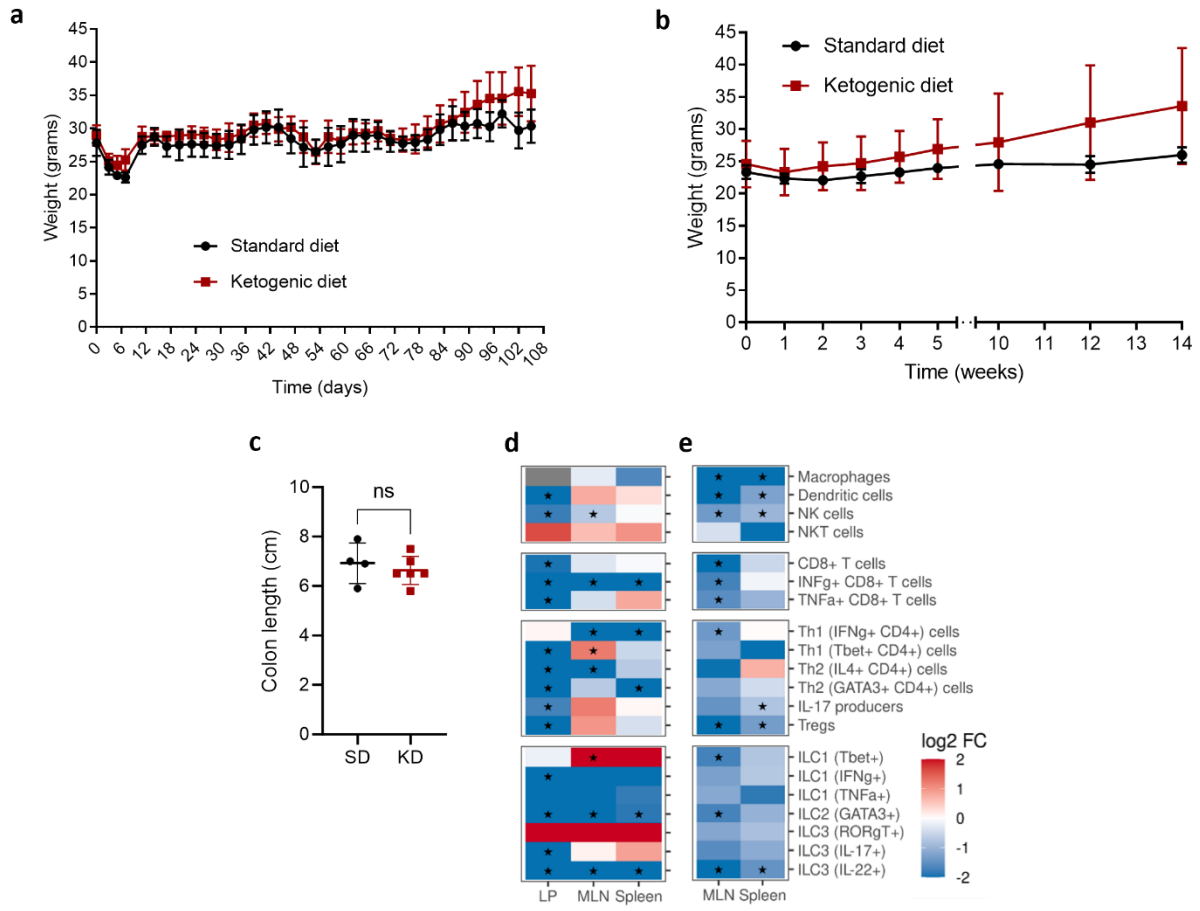

465

466 **Extended data figure 2. | a-b.** Mouse body weight (grams) over time (weeks) in the SPF (**a**) and GF (**b**)

467 dietary experiments. Weight was not recorded between week five and ten as no scale was available in the

468 facility. **c.** Colon length (cm) in the GF dietary experiment at experimental endpoint. **d-e.** Heatmap of KD-

469 induced changes in the immune cell compartment in relation to SD (log2foldchange) in the SPF (**h**) and GF

470 (**i**) diet experiments. Stars overlaid on the heatmaps indicate *p<0.05, least squared means analysis. Data

471 is shown as mean±SD in (**a**), (**b**) and (**c**). Mann-Whitney U in (**c**), * p<0.05, ** p<0.01, *** p<0.001. Data in

472 (**a**) shows n=8 and 9 mice in the KD-fed condition and the SD-fed condition respectively, pooled from two

473 independent experiments in the SPF facility. Data in (**b**), (**c**), (**d**), and (**e**) shows n=4 mice in the SD-fed

474 condition and n=6 mice in the KD-fed condition from one experiment in the GF facility.

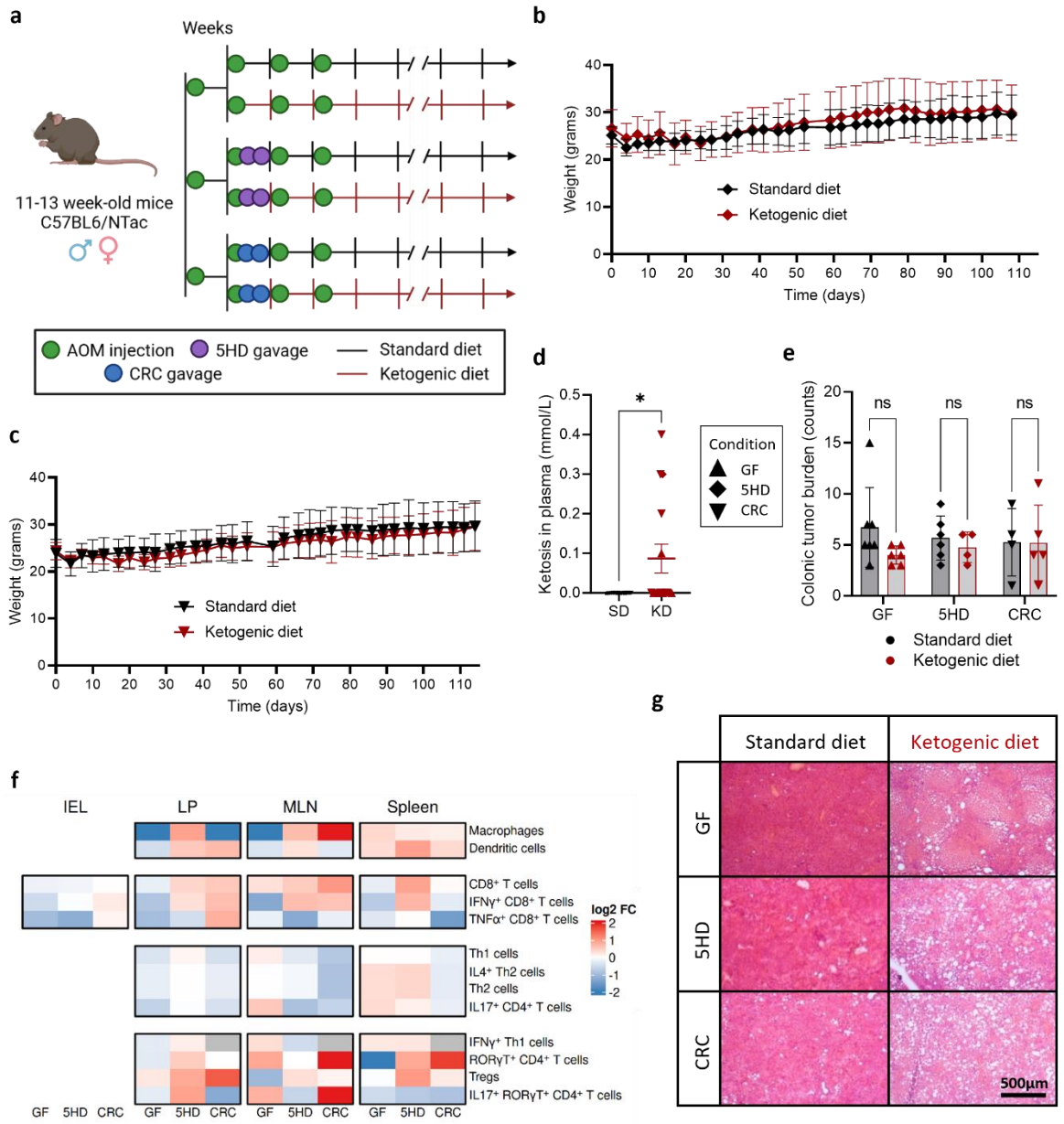

475

476 **Extended data figure 3. | a.** Schematic representation of the dietary AOM experimental setup in the GF

477 facility (created with BioRender.com). **b-c.** Mouse body weight (grams) over time (days) in mice

478 administered 5HD (**b**) and CRC (**c**). **d.** Ketosis levels in plasma (mmol/L), measured using a handheld

479 ketometer. **e.** Colonic tumor burden at endpoint. **f.** Heatmap of immune cell population phenotyping of

480 intra-epithelial lymphocytes (IEL), lamina propria (LP), mesenteric lymph nodes (MLN) and spleens of KD-
481 fed mice in relation to SD-fed mice in GF mice (GF), in mice gavaged with a mixture of stool samples from
482 five healthy donors (5HD), and in mice gavaged with stool from a single CRC patient (CRC). Least-squared
483 means analysis was performed on each combination of tissue and cell immune cell type using a linear
484 model, however no statistically significant differences were found. **g.** One representative image of a
485 section of liver stained with H&E per condition. Scale bar=500µm. Data in (**b**), (**c**), (**d**) and (**e**) shown as
486 mean±SD. Mann-Whitney U test in (**d**) and (**e**), not significant (ns), * $p<0.05$, ** $p<0.01$, *** $p<0.001$. Data
487 in (**b**), (**c**), (**d**), (**e**) and (**f**) shows n=7 and 6 mice in the GF SD and KD conditions respectively, n=6 and 4
488 mice in the 5HD SD and KD conditions respectively, and n=4 and 5 mice in the CRC SD and KD conditions
489 respectively.

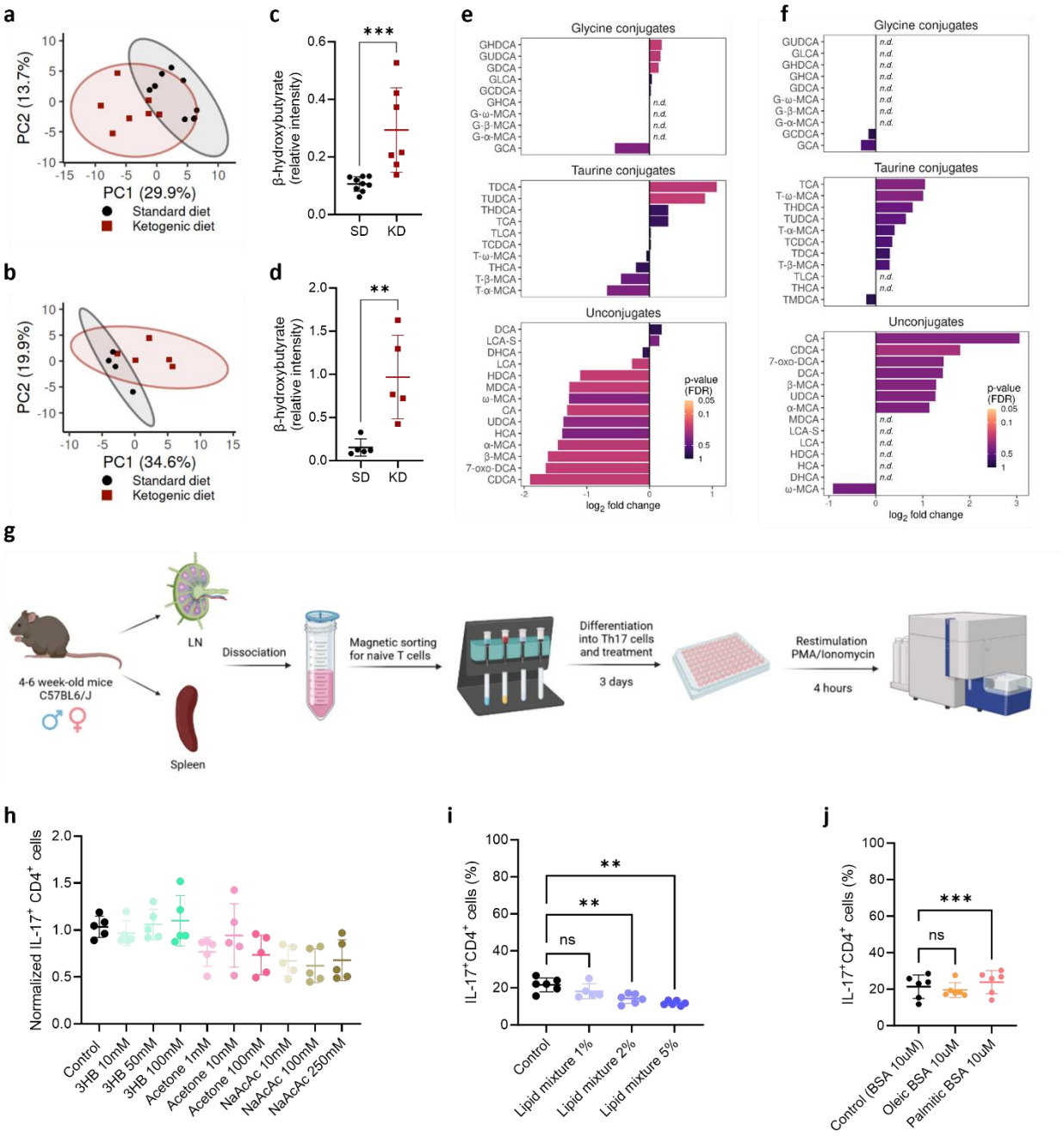

490

491 **Extended data figure 4. | a-b.** PCA (95% confidence interval) of plasma metabolites from mice in the SPF

492 (**a**) and GF (**b**) diet experiments, as analyzed by united GC-MS and LC-MS analyses (**a**) and GC-MS analysis

493 alone (**b**). **c-d.** Relative intensity of β-HB in plasma from mice in the SPF (**c**) and GF (**d**) diet experiments,

494 as analyzed by GC-MS. **e-f.** Log_2foldchange of identified plasma bile acids in KD-fed mice in relation to SD-

495 fed mice in the SPF (**e**) and GF (**f**) facilities, as analyzed UHPLC-MS. **g.** Schematic representation of the
496 experimental setup of a Th17 cell differentiation assay (created with BioRender.com). **h-j.** Th17
497 differentiation upon treatment with β-HB (10mM, 50mM, 100mM), acetone (1mM, 10mM, 100mM) or
498 sodium acetoacetate (10mM, 100mM, 250mM) in (**h**), a lipid mixture (1%, 2%, 5%) in (**i**), BSA-complexed
499 palmitic and oleic acid (10µm) in (**j**). Data in (**c**), (**d**), (**h**), (**i**) and (**j**) is shown as mean±SD. Two-tailed Mann-
500 Whitney U test in (**c**) and (**d**); Two-tailed unpaired T test with FDR correction in (**e**) and (**f**); Paired ordinary
501 one-way ANOVA in (**h**), (**i**) and (**j**); ns=not significant, * $p<0.05$, ** $p<0.01$, *** $p<0.001$. Paired ordinary
502 one-way ANOVA comparing each set of ketone body dilutions to the control yielded no statistical
503 significance in (**h**). Data in (**a**), (**c**) and (**e**) shows n=9 mice in the SD-fed condition and n=8 mice in the KD-
504 fed condition. Data in (**b**), (**d**) and (**f**) shows n=4 mice in the SD-fed condition and n=5 mice in the KD-fed
505 condition. n=6 mice in (**c**) and (**d**); n=5 mice in (**e**). Abbreviations: not detected (n.d.), cholic acid (CA),
506 hyocholic acid (HCA), chenodeoxycholic acid (CDCA), deoxycholic acid (DCA), 7-oxo-deoxycholic acid (7-
507 oxo-DCA), murideoxycholic acid (MDCA), lithocholic acid (LCA), ursodeoxycholic acid (UDCA),
508 hyodeoxycholic acid (HDCA), muricholic acids (α-MCA, β-MCA and ω-MCA), taurocholic acid (TCA),
509 taurohyocholic acid (THCA), taurochenodeoxycholic acid (TCDCA), taurodeoxycholic acid (TDCA),
510 taurolithocholic acid (TLCA), tauroursodeoxycholic acid (TUDCA), taurohyodeoxycholic acid (THDCA),
511 tauro-α-muricholic acid (T-α-MCA), tauro-β-muricholic acid (T-β-MCA) and tauro-ω-muricholic acid (T-ω-
512 MCA).

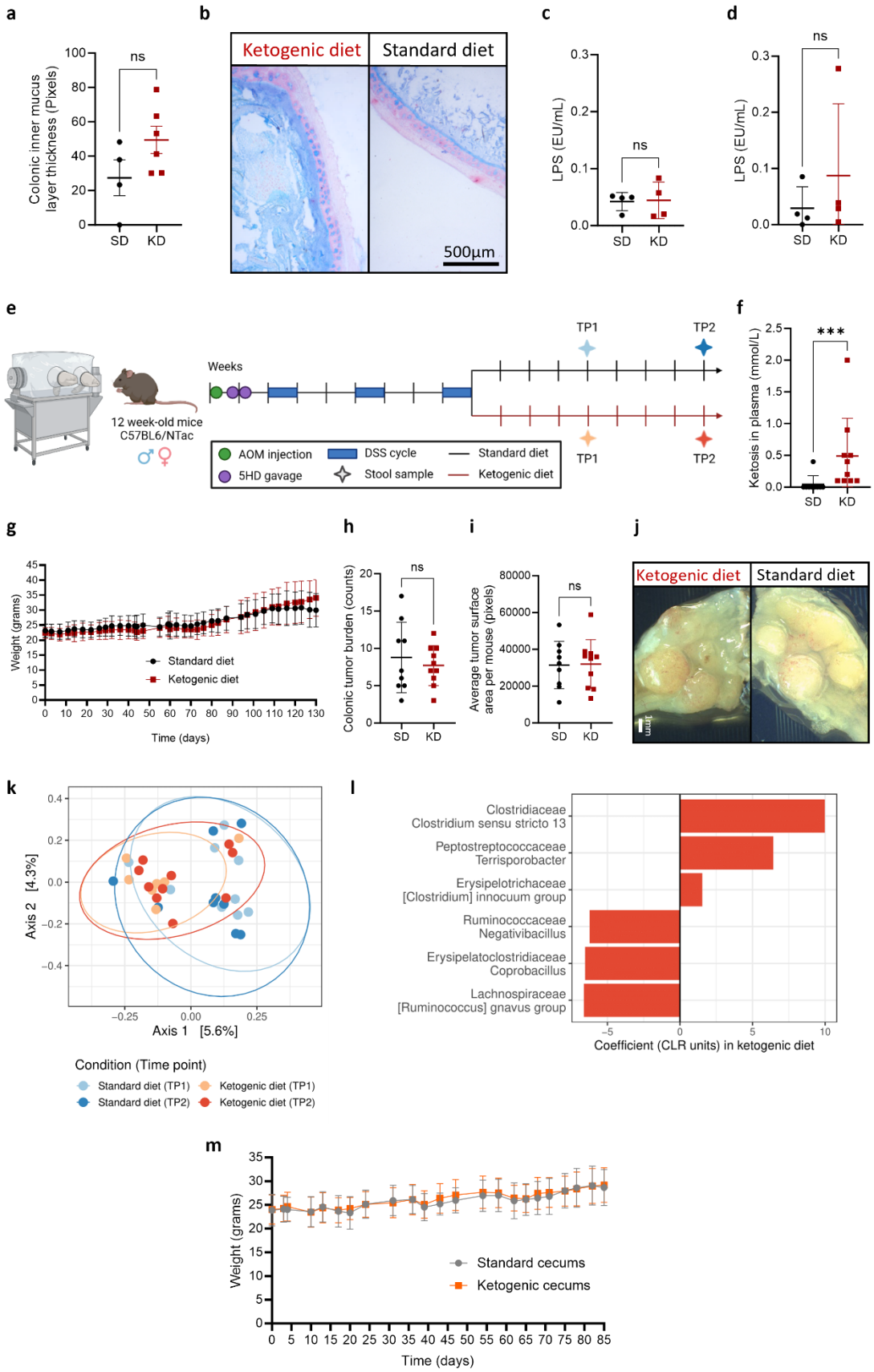
a
Colonic inner mucus layer thickness (Pixels)
ns
SD
KD
b
Ketogenic diet
Standard diet
500µm
c
LPS (EU/mL)
ns
SD
KD
d
LPS (EU/mL)
ns
SD
KD
e
12 week-old mice
C57BL6/NTac
Weeks
TP1
TP2
AOM injection
5HD gavage
DSS cycle
Stool sample
Standard diet
Ketogenic diet
f
Ketosis in plasma (mmol/L)
***
SD
KD
g
Weight (grams)
Standard diet
Ketogenic diet
Time (days)
h
Colonic tumor burden (counts)
ns
SD
KD
i
Average tumor surface area per mouse (pixels)
ns
SD
KD
j
Ketogenic diet
Standard diet
2mm
k
Axis 2 [4.3%]
Axis 1 [5.6%]
Condition (Time point)
Standard diet (TP1)
Ketogenic diet (TP1)
Standard diet (TP2)
Ketogenic diet (TP2)
l
Clostridiaceae
Clostridium sensu stricto 13
Peptostreptococcaceae
Terrisporobacter
Erysipelotrichaceae
[Clostridium] innocuum group
Ruminococcaceae
Negativibacillus
Erysipelatoclostridiaceae
Coprobacillus
Lachnospiraceae
[Ruminococcus] gnavus group
Coefficient (CLR units) in ketogenic diet
m
Weight (grams)
Standard cecums
Ketogenic cecums
Time (days)

513

514 **Extended data figure 5. | a-b.** Colonic inner mucus layer thickness (in pixels, **a**) and representative images
515 of Alcian Blue staining of colonic cryosections (**b**) in GF KD-fed and SD-fed mice. **c-d.** LPS (endotoxin units
516 (EU) per milliliter) in plasma from GF (**c**) and SPF (**d**) KD-fed mice and SD-fed mice measured by ELISA.
517 Panels **a-d** relate to experiments shown in Fig. 1. **e.** Schematic representation of the experimental setup
518 in the GF facility, in which mice were housed in open-top cages in a gnotobiotic flexible-film isolator
519 (created with Biorender.com). **f.** Ketosis levels in mouse plasma (mmol/L), measured using a handheld
520 ketometer. **g.** Mouse body weight (grams) over time (weeks). **h-j.** Colonic tumor burden (**h**), average
521 tumor surface area per mouse (pixels, **i**) and representative images of colonic tumors, scale bar=1mm (**j**)
522 from mice at experimental endpoint. **k.** β-diversity as assessed by PCoA of Bray-Curtis distance in mouse
523 fecal samples collected at two time points. **l.** Differentially abundant bacterial families (coefficient, CLR
524 units) in mouse fecal samples, estimated using a generalized linear model on CLR data (p.adj<0.05
525 (Benjamini-Hochberg correction), max. abundance>0.05), with the standard diet condition as the
526 reference. **m.** Mouse body weight (grams) over time (days) in the CMT experiment. Data is shown as
527 mean±SD in (**a**), (**c**), (**d**), (**f**), (**g**), (**h**), (**i**) and (**m**). Two-tailed Mann-Whitney U test in (**a**), (**c**), (**d**), (**f**), (**h**) and
528 (**i**); * p<0.05, ** p<0.01, *** p<0.001. Data in (**a**), (**c**) and (**d**) shows n=4 mice per condition. Data in (**f**), (**g**),
529 (**h**), (**i**), (**k**) and (**l**) shows n=9 mice in the SD-fed condition and n=8 mice in the KD-fed condition, pooled
530 from two independent experiments. Data in (**m**) shows 16 mice per condition.

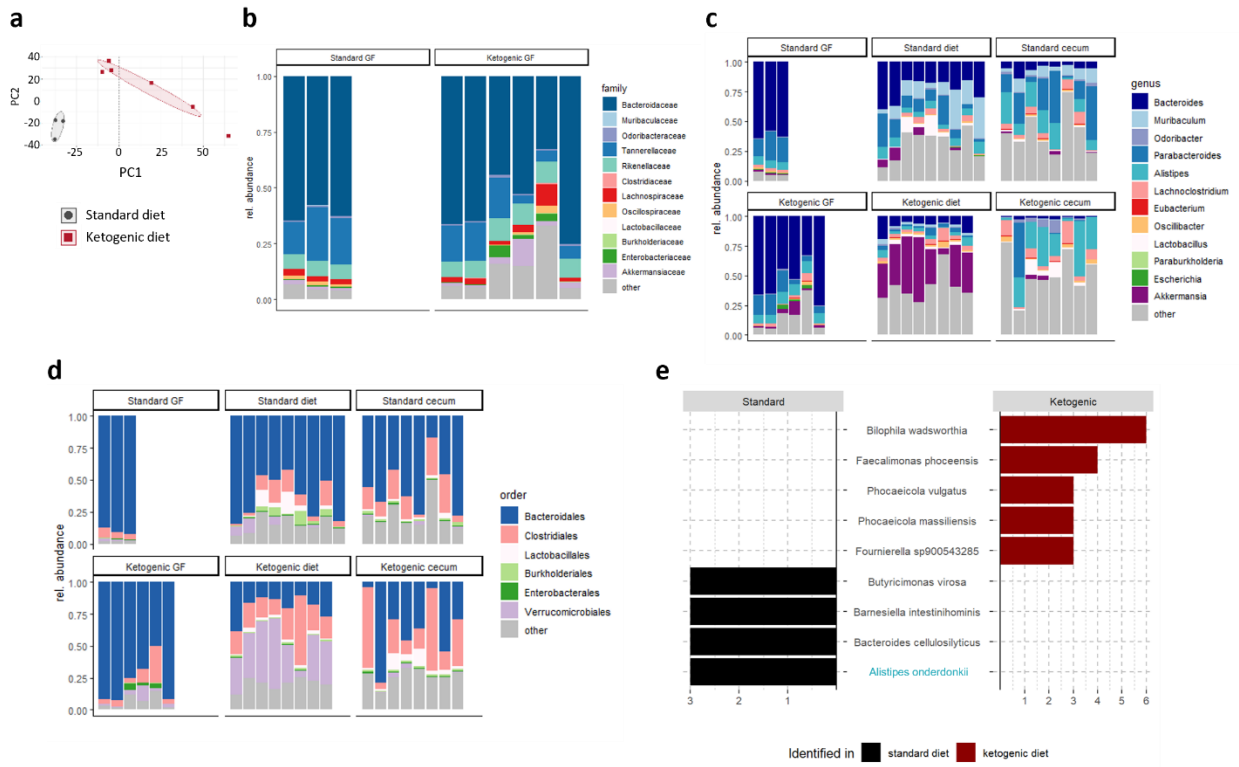

Extended data figure 6. | a. PCA of WGS sequencing of fecal samples collected at endpoint from GF KD and SD-fed mice. **b.** Relative abundance of bacterial families detected in fecal samples from GF KD- and SD-fed mice at endpoint, as analyzed by WGS. **c-d.** Relative abundance of bacterial genera (**c**) and orders (**d**) detected in fecal samples collected at endpoint from GF and SPF KD- and SD-fed mice, as well as KC and SC recipient mice, as analyzed by WGS. **e.** Highly characteristic bacterial MAGs (detected in at least three mice in one condition but not more than two mice in the other), detected in GF KD- and SD-fed murine fecal samples at endpoint, as analyzed by WGS. Data shows samples collected from n=9 SPF SD-fed mice and n=8 SPF KD-fed mice, pooled from two independent experiments in (**c**) and (**d**); n= 8 KC and n=8 SC recipient mice from one experiment in (**c**) and (**d**); n=3 GF SD and n=6 GF KD mice from one experiment in (**a**), (**b**) and (**e**).

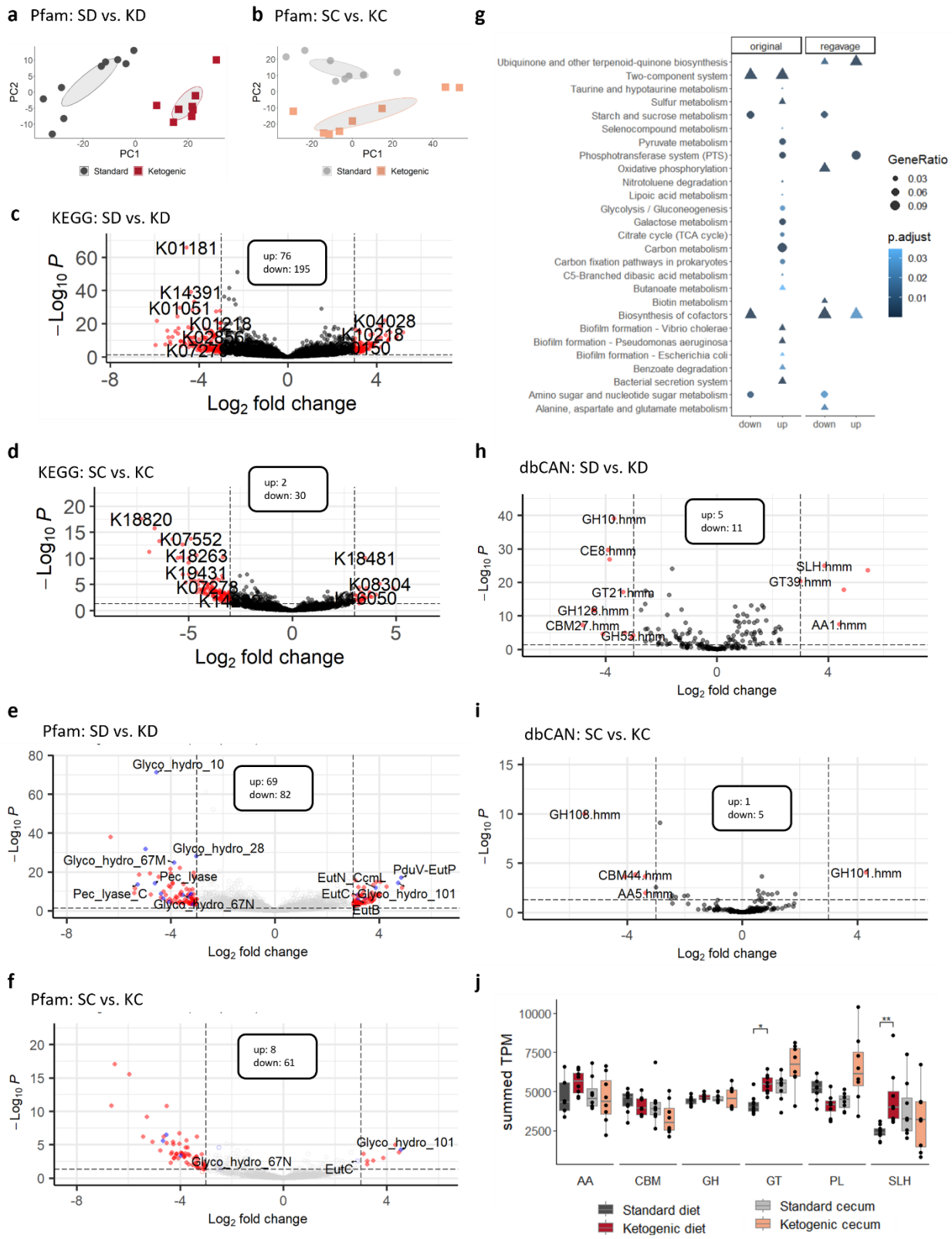
a Pfam: SD vs. KD
b Pfam: SC vs. KC
PC1
PC2
Standard
Ketogenic
c KEGG: SD vs. KD
up: 76
down: 195
K01181
K14391
K01051
K01218
K02856
K07278
K04028
K10218
K01150
−Log10 P
Log2 fold change
d KEGG: SC vs. KC
up: 2
down: 30
K18820
K07552
K18263
K19431
K07278
K18481
K08304
K16050
e Pfam: SD vs. KD
up: 69
down: 82
Glyco_hydro_10
Glyco_hydro_28
Glyco_hydro_67M
Pec_lyase
Pec_lyase_C
Glyco_hydro_67N
EutN_CcmL
EutC
EutB
PduV-EutP
Glyco_hydro_101
f Pfam: SC vs. KC
up: 8
down: 61
Glyco_hydro_67N
EutC
Glyco_hydro_101
g
original
regavage
Ubiquinone and other terpenoid-quinone biosynthesis
Two-component system
Taurine and hypotaurine metabolism
Sulfur metabolism
Starch and sucrose metabolism
Selenocompound metabolism
Pyruvate metabolism
Phosphotransferase system (PTS)
Oxidative phosphorylation
Nitrotoluene degradation
Lipoic acid metabolism
Glycolysis / Gluconeogenesis
Galactose metabolism
Citrate cycle (TCA cycle)
Carbon metabolism
Carbon fixation pathways in prokaryotes
C5-Branched dibasic acid metabolism
Butanoate metabolism
Biotin metabolism
Biosynthesis of cofactors
Biofilm formation - Vibrio cholerae
Biofilm formation - Pseudomonas aeruginosa
Biofilm formation - Escherichia coli
Benzoate degradation
Bacterial secretion system
Amino sugar and nucleotide sugar metabolism
Alanine, aspartate and glutamate metabolism
down
up
down
up
GeneRatio
0.03
0.06
0.09
p.adjust
0.03
0.02
0.01
h dbCAN: SD vs. KD
up: 5
down: 11
GH10.hmm
CE8.hmm
GT21.hmm
GH128.hmm
CBM27.hmm
GH55.hmm
SLH.hmm
GT39.hmm
AA1.hmm
i dbCAN: SC vs. KC
up: 1
down: 5
GH108.hmm
CBM44.hmm
AA5.hmm
GH101.hmm
j
summed TPM
AA
CBM
GH
GT
PL
SLH
Standard diet
Ketogenic diet
Standard cecum
Ketogenic cecum

542

543 **Extended data figure 7. | a-b.** PCA (95% confidence interval) of the predicted functional features of the
544 gut microbiome (Pfam) of KC and SC recipient mice at endpoint. **c-f.** Differences in gene expression profiles
545 mapped to the KEGG (**e** and **f**) and Pfam (**g** and **h**) databases detected in fecal samples from KD- and SD-
546 fed mice (**c** and **d**), and KC and SC recipient mice (**e** and **f**), at endpoint. Blue data points in (**e**) and (**f**)
547 represent carbohydrate-metabolism-related Pfams, solid data points represent Pfams above both defined
548 thresholds, while empty datapoints represent Pfams below these thresholds. Pfams named in (**e**) overlap
549 with those named in (**d**). **g.** Overrepresentation analysis (KEGG, threshold log2FC > 2, p.adj. < 0.05) of
550 genes detected in fecal samples collected at endpoint from SPF KD- and SD-fed mice, and KC and SC
551 recipient mice. Gene sets related to energy metabolism are shown as circular data points, while all other
552 gene sets are shown as triangular data points. Data point size corresponds to gene ratio. **h-i.** Differences
553 in gene expression profiles mapped to the DBcan database detected in fecal samples from KD- and SD-fed
554 mice (**h**), and KC and SC recipient mice (**i**) at endpoint. **j.** Abundance of main CAZyme families (summed
555 transcripts per million (TPM)) in fecal samples from KD- and SD-fed mice, and KC and SC recipient mice, at
556 endpoint. Boxplots show medians with 1st and 3rd quantiles. The whiskers from the hinges to the
557 smallest/largest values represent 1.5*inter-quartile range (IQR). Wilcoxon signed-rank test with Holm
558 correction, ns $p > 0.05$, * $p \leq 0.05$, ** $p \leq 0.01$, *** $p \leq 0.001$, **** $p \leq 0.0001$. Abbreviations: auxiliary
559 activities (AA), carbohydrate binding molecule (CBM), glycoside hydrolase (GH), glycosyl transferase (GT),
560 polysaccharide lyase (PL) and S-layer homology (SLH) families. In (**c**), (**d**), (**e**), (), (**h**) and (**j**), the horizontal
561 lines correspond to a three-fold increase (right) or decrease (left) in KD in relation to SD, in KC in relation
562 SC. The vertical lines correspond to $p<0.05$, the defined cutoff for statistical significance (DESeq2). Red
563 data points represent statistically significantly ($p<0.05$) differentially expressed genes with three-fold up-
564 or down-regulation. Data shows n=8 SPF KD-fed mice and n=9 mice SPF SD-fed mice, pooled from two
565 independent experiments, and n=8 KC and n=8 SC recipient mice from one experiment.

566

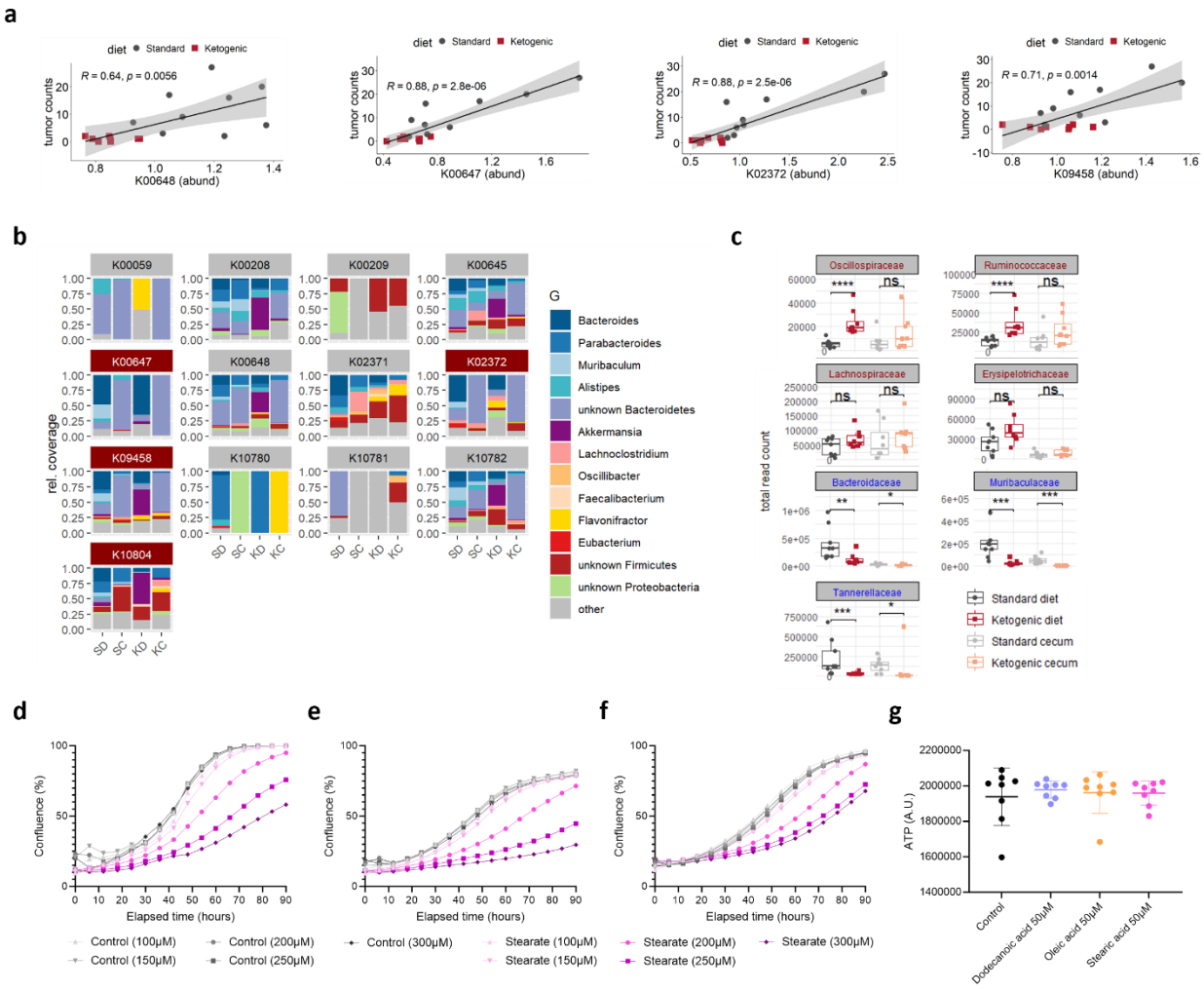

Extended data figure 8. | a. Correlation (Pearson) between colonic tumor burden of KD and SD-fed mice and the selected KOs of interest K00647, K00648, K02372 and K09458. **b.** Relative taxonomic assignment of contigs encoding for the selected KOs of interest at genus level in fecal samples from KD- and SD-fed mice, and KC and SC recipient mice, at endpoint. The abundance of KOs highlighted in red correlates with colonic tumor burden in KD- and SD-fed mice. **c.** Relative abundance (total read counts) of selected families of interest detected in murine fecal samples from KD-, SD-fed, KC and SC recipient mice at endpoint**.** Members of the class Clostridia are listed in red, while members of the class Bacteroidia are listed in blue. Boxplots show medians with 1st and 3rd quantiles. The whiskers from the hinges to the smallest/largest values represent 1.5*inter-quartile range (IQR). Wilcoxon signed-rank test with

577 Bonferroni correction, ns $p > 0.05$, * $p \leq 0.05$, ** $p \leq 0.01$, *** $p \leq 0.001$, **** $p \leq 0.0001$. **d-f.** HCT 116
578 (**d**), HT29 (**e**) and Caco2 (**f**) proliferation over time after treatment with stearic acid or control (100µM,
579 150 µM, 200 µM, 250 µM, 300 µM). Data shows mean of n=3 independent experiments (**d** and **e**), or n=2
580 independent experiments (**f**), each with eight technical replicates per condition. **g.** ATP measurement
581 (CellTiterGlo) of HT29 cells at 72 hours after treatment with stearic acid, oleic acid, dodecanoic acid or
582 control (200 µM). Data shows n=8 technical replicates from one experiment. Data shown in (**a**), (**b, SD and**
583 **KD**) and (**c, red and black**) are from n=9 SPF SD-fed and n=8 SPF KD-fed mice, pooled from two
584 independent experiments. Data shown in (**b, SC and KC**) and (**c, gray and orange**) are from n=8 mice per
585 condition.

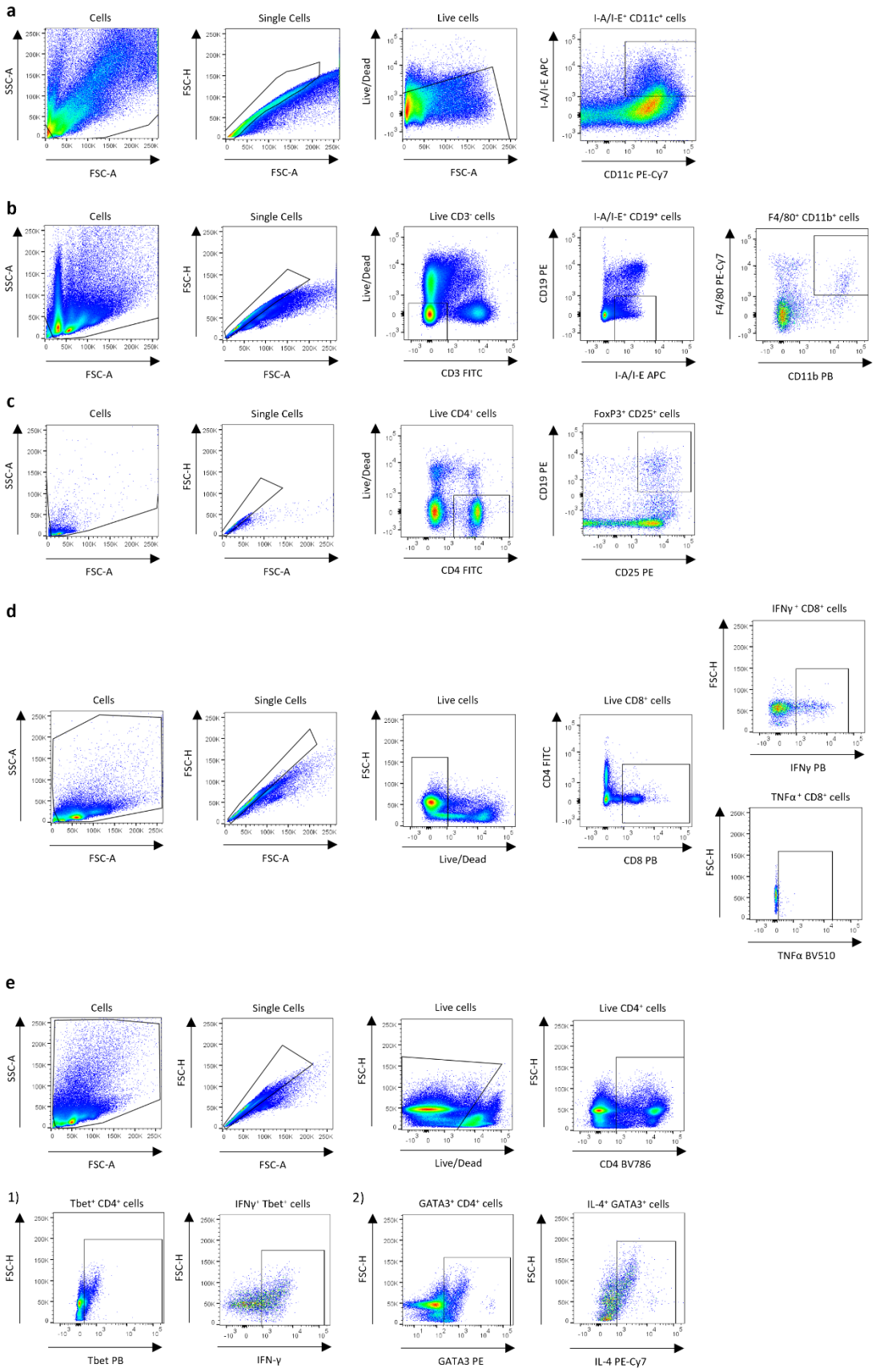
a
Cells
SSC-A
FSC-A
Single Cells
FSC-H
FSC-A
Live cells
Live/Dead
FSC-A
I-A/I-E⁺ CD11c⁺ cells
I-A/I-E APC
CD11c PE-Cy7
b
Cells
SSC-A
FSC-A
Single Cells
FSC-H
FSC-A
Live CD3⁻ cells
Live/Dead
CD3 FITC
I-A/I-E⁺ CD19⁺ cells
CD19 PE
I-A/I-E APC
F4/80⁺ CD11b⁺ cells
F4/80 PE-Cy7
CD11b PB
c
Cells
SSC-A
FSC-A
Single Cells
FSC-H
FSC-A
Live CD4⁺ cells
Live/Dead
CD4 FITC
FoxP3⁺ CD25⁺ cells
CD19 PE
CD25 PE
d
Cells
SSC-A
FSC-A
Single Cells
FSC-H
FSC-A
Live cells
FSC-H
Live/Dead
Live CD8⁺ cells
CD4 FITC
CD8 PB
IFNγ⁺ CD8⁺ cells
FSC-H
IFNγ PB
TNFα⁺ CD8⁺ cells
FSC-H
TNFα BV510
e
Cells
SSC-A
FSC-A
Single Cells
FSC-H
FSC-A
Live cells
FSC-H
Live/Dead
Live CD4⁺ cells
FSC-H
CD4 BV786
1)
Tbet⁺ CD4⁺ cells
FSC-H
Tbet PB
IFNγ⁺ Tbet⁺ cells
FSC-H
IFN-γ
2)
GATA3⁺ CD4⁺ cells
FSC-H
GATA3 PE
IL-4⁺ GATA3⁺ cells
FSC-H
IL-4 PE-Cy7

586

587 **Extended data figure 9. | a.** Representative gating strategy of dendritic cells. **b.** Representative gating
588 strategy of macrophages. **c.** Representative gating strategy of regulatory T cells. **d.** Representative gating
589 strategy of $CD8^+$ T cells. **e.** Representative gating strategy of T helper 1 (subpanel 1) and T helper 2 cells
590 (subpanel 2).

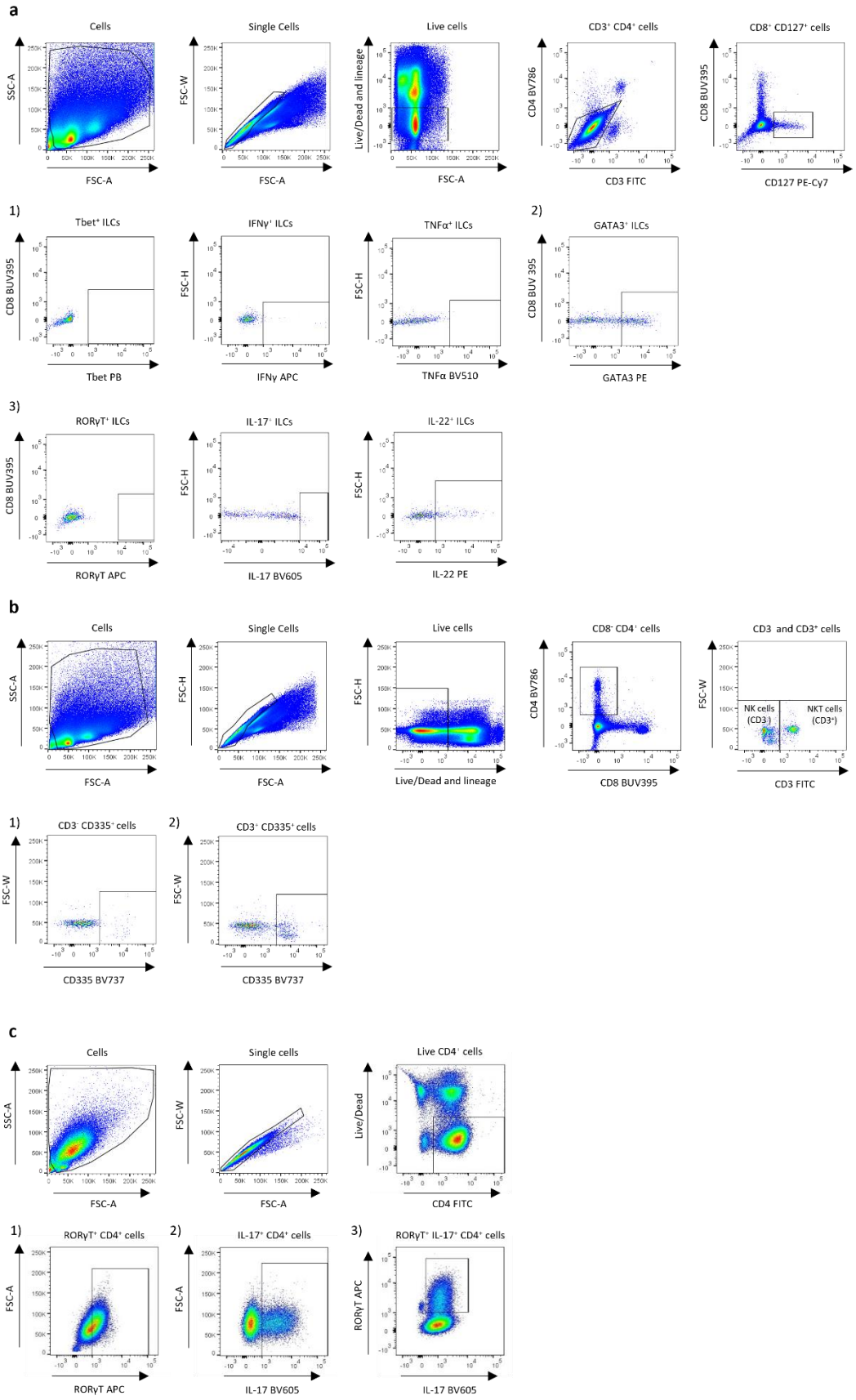
a
Cells
SSC-A
FSC-A
Single Cells
FSC-W
FSC-A
Live cells
Live/Dead and lineage
FSC-A
CD3⁺ CD4⁺ cells
CD4 BV786
CD3 FITC
CD8⁺ CD127⁺ cells
CD8 BUV395
CD127 PE-Cy7
1)
Tbet⁺ ILCs
CD8 BUV395
Tbet PB
IFNγ⁺ ILCs
FSC-H
IFNγ APC
TNFα⁺ ILCs
FSC-H
TNFα BV510
2)
GATA3⁺ ILCs
CD8 BUV 395
GATA3 PE
3)
RORγT⁺ ILCs
CD8 BUV395
RORγT APC
IL-17⁺ ILCs
FSC-H
IL-17 BV605
IL-22⁺ ILCs
FSC-H
IL-22 PE
b
Cells
SSC-A
FSC-A
Single Cells
FSC-H
FSC-A
Live cells
FSC-H
Live/Dead and lineage
CD8⁻ CD4⁺ cells
CD4 BV786
CD8 BUV395
CD3 and CD3⁺ cells
FSC-W
NK cells (CD3⁻)
NKT cells (CD3⁺)
CD3 FITC
1)
CD3⁻ CD335⁺ cells
FSC-W
CD335 BV737
2)
CD3⁺ CD335⁺ cells
FSC-W
CD335 BV737
c
Cells
SSC-A
FSC-A
Single cells
FSC-W
FSC-A
Live CD4⁺ cells
Live/Dead
CD4 FITC
1)
RORγT⁺ CD4⁺ cells
FSC-A
RORγT APC
2)
IL-17⁺ CD4⁺ cells
FSC-A
IL-17 BV605
3)
RORγT⁺ IL-17⁺ CD4⁺ cells
RORγT APC
IL-17 BV605

591

592 **Extended data figure 10. | a.** Representative gating strategy of innate lymphoid cells (ILC) - ILC1 (subpanel
593 1), ILC2 (subpanel 2), ILC3 (subpanel 3). Transcription factors and cytokines are stained in two separate
594 batches. **b.** Representative gating strategy of natural killer (subpanel 1) and natural killer T (subpanel 2)
595 cells. **c.** Representative gating strategy of T helper 17 cells – transcription-factor-based phenotyping
596 (subpanel 1), cytokine-based phenotyping (subpanel 2) and the combined strategy (subpanel 3).
597

598 **Acknowledgments**

599 We acknowledge the contributions of the following people in the context of this project and thank
600 them for their work: Dominik Ternes, Rubens Begaj, Martin Nurmik and Cedric Gilson (MDM group,
601 DLSM) for assistance during organ processing at experimental endpoint; Ysaline Bossicard (MDM group,
602 DLSM) for tissue cryosectioning; Stephanie Willieme, Eric Grant and Mahesh Desai (LIH) for processing of
603 murine fecal samples; Xiangyi Dong, Floriane Gavotto and Christian Jäger (LCSB Metabolomics Platform)
604 for metabolite profile acquisition and raw data analysis; Aurélien Ginolhac (DLSM) for contributions to
605 data pre-processing; Pau Perez Escriva (DLSM) for bacterial culturing; Giulia Cesi (DLSM) for her
606 contributions to obtaining funding; Djalil Coowar, Jennifer Behm, Julie Virolle, Cloe Ordrenneau and all
607 other members of the Animal Facility Team (LCSB); Sara Gomez and Eliane Klein (DLSM) for maintenance
608 of organoid cultures and organoid experimentation; Rashi Halder for fecal sample 16s and WGS
609 sequencing. The sequencing experiments presented in this paper were carried out at the LCSB sequencing
610 platform (RRID: SCR_021931) at the University of Luxembourg. We also thank the patients who
611 contributed their samples to the national colorectal cancer cohort from which we obtained the samples
612 used in this study, as well as Christelle Bahlawane (CIEC), Eve Herkenne (CIEC), Laetitia Garcia (CIEC), Ingrid
613 Vreja (CIEC), and nurses from CIEC for contributing to this cohort. We thank Dr. Barbara Kofler for her
614 feedback and discussions during the course of the project. The experiments presented in this paper were

carried out using the high-performance computing facilities at the University of Luxembourg (https://hpc.uni.lu)[56]. BioRender (BioRender.com) was used for graphical illustration.

Funding

This work was supported by the Luxembourg National Research Fund (FNR) (grant nos. CORE/C16/BM/11282028 (E.L.), PoC/18/12554295 (E.L.), PRIDE17/11823097 (M.T., M.K., L.d.N.) and CORE/15/BM/10404093 (P.W.)), by the Luxembourg National Research Fund and the Fondation Cancer Luxembourg (grant no. CORE/C20/BM/14591557 (E.L.)) as well as by the Fondation du Pélican de Mie and Pierre Hippert-Faber under the aegis of the Fondation de Luxembourg ('Pelican Grant'; M.T. and M.M.), a FNRS-Télévie grant to M.M., no. 7.4565.21-40007364), an Internal Research Project at the University of Luxembourg (MiDiCa—integrated analysis of the effects of microbiome-diet interactions on human colorectal adenocarcinoma enterocytes; E.L., P.W. and S.H.), the Fondation Cancer and the Fondation Kriibskrank Kanner Luxembourg (V.I.P), the Action LIONS Vaincre le Cancer Luxembourg and a European Research Council grant under the European Union's Horizon 2020 research and innovation programme (grant agreement no. 863664 to P.W.). This project was also supported by the Doctoral School in Science and Engineering (M.T., M.K., M.M. and L.d.N.) and the Department of Life Sciences and Medicine at the University of Luxembourg. The funders had no role in study design, data collection and analysis, decision to publish or preparation of the manuscript.

637 **Methods**

638 *Human sample collection*

639 Human samples were obtained and handled in accordance with institutional guidelines. All human
640 samples used in this project were donated freely, upon informed consent. Ethical approval was given by
641 the Comité National d'Ethique de Recherche of Luxembourg (SOCS authorization number 201009/09 and
642 MuSt authorization number 201110/05) and the National Commission for Data Protection in Luxembourg.
643 Stool samples were collected at the donors' homes. The CRC patient stool sample (SOCS) was collected
644 prior to surgery, immediately snap-frozen in a dryshipper and stored at -150°C until processing. Healthy
645 donor stool samples (MuSt) were collected at the donors' homes in accordance with the standard
646 practices established by the Integrated Biobank of Luxembourg (IBBL), frozen and transported on dry ice
647 to the IBBL, then thawed for mixing and aliquoting, then refrozen and stored at -80°C until processing.

648

649 *In vivo mouse experiments*

650 Animal experiments were performed according to all applicable laws and regulations, with
651 approval from the Animal Experimentation Ethics Committee (AEEC) and the veterinary service of the
652 Ministry of Agriculture, Viticulture and Rural Development of Luxembourg (LUPA2019-13). They ensure
653 that the care and the use of the animals for research purposes is conducted according to the European
654 Union Directive 2010/63/EU and to the Grand-Ducal Regulation of the 11th of January 2013, regarding
655 the protection of animals used for experimentation. This includes justification for the use of the animals,
656 guidelines for their care and welfare, and the incorporation of the 3Rs (replacement, reduction and
657 refinement). All animal protocols were reviewed by a biostatistician.

658

659

660

661 Highly inflammatory mouse model of CRC

662 SPF mice were administered a sterile-filtered antibiotic mix (vancomycin hydrochloride
663 (500mg/L), ampicillin (1g/L), neomycin (1g/L) and metronidazole (1g/L)) via their drinking water for one
664 week (refreshed every other day). GF, SPF, and CMT mice were administered a single intraperitoneal
665 injection of sterile-filtered AOM (10mg/kg mouse body weight in PBS, Sigma). After AOM injection, GF
666 mice received a gastric gavage of 5HD on two subsequent days, while SPF mice were subjected to bi-
667 weekly FMT during the induction of CRC to maintain enrichment of the donor fecal microbiome in relation
668 to the residual host mouse microbiome. FMT in SPF mice was ceased at diet change, upon removal of the
669 third cycle of DSS, to allow for a natural evolution of the gut microbiome in response to the diet and CRC
670 progression. CMT mice received a gastric gavage on two subsequent days after AOM injection, between
671 each cycle of DSS and once weekly after the last cycle of DSS. Three days after the first FMT/CMT, GF, SPF
672 and CMT mice were administered DSS via their drinking water. Mice were administered a total of three
673 cycles of DSS, with a two-week-long recovery period between each cycle. In the dietary experiments, half
674 of the mice were maintained on standard diet (A04, SAFE Lab, 40kGy irradiation) and half were randomly
675 allocated to the ketogenic diet (S0382-E210, ssniff Spezialdiäten, 25Gy) at the end of the last cycle of DSS.
676 CMT mice were all maintained on standard diet for the duration of the experiment. Collected stool
677 samples were snap-frozen in liquid nitrogen and stored at -80°C until use. Further details can be found in
678 the supplementary methods file available online.

679

680 Lowly inflammatory mouse model of CRC.

681 Mice were administered four intraperitoneal injections of sterile-filteretd AOM (15mg/kg mouse
682 body weight in PBS), once per week for four weeks, then gastrically gavaged with 5HD, a single CRC patient
683 stool sample (CRC), or fecal suspension buffer on two subsequent days. Mice gavaged with 5HD mix and
684 CRC were housed in individually ventilated cages, while suspension-buffer-gavaged mice were housed in

685 open-top cages in a gnotobiotic flexible-film isolator and were not weighed to avoid contamination. Half
686 of the mice were randomly allocated to the KD one week after the first injection of AOM.
687
688 *16s rRNA sequencing data analysis*
689 Raw 16S rRNA gene sequences (FASTAQ files) were cleaned and clustered as operational
690 taxonomic units (OTU) using the Dada2 pipeline[57] and using silvia train set (versions 132 to 138) for
691 taxonomy inference. Samples with no reads, amplicon sequence variants (ASV) with no identified phylum
692 or class and taxa present in less than 5% of samples were excluded where necessary. Data was aggregated
693 to genus level and relative abundances were computed, or centered log-ratio (CLR) transformation[58] was
694 performed. Differential analysis and graphical representation were performed in R, using the packages
695 from Bioconductor (DESeq2[59], phyloseq[60]) and tidyverse (ggplot).
696
697 *WGS data analysis for human fecal samples*
698 Raw genome sequences (FASTQ files) were cleaned using the Sunbeam pipeline[61]. Function
699 profiling was performed with HUMAnN Version 3.0[62] using the quality-controlled and host-
700 decontaminated FASTQ files obtained from Sunbeam. Graphical representation was performed in R, using
701 the packages from tidyverse, broom and RColorBrewer.
702
703 *WGS data analysis for mouse fecal samples*
704 The Integrated Meta-omic Pipeline (IMP; v3 - commitID #6f1badf7)[63] was used to process paired
705 forward and reverse reads using the built-in metagenomic workflow. The workflow includes pre-
706 processing, assembly, genome reconstruction and functional annotation of genes based on custom
707 databases in a reproducible manner. *De Novo* assembly was performed using the MEGAHIT (version 2.0)
708 assembler. Default IMP parameters were retained for all samples. MetaBAT2 and MaxBin2 in addition to

709 binny[64] were used for binning and genome reconstructions, i.e. MAGs. Subsequently, we obtained a non-
710 redundant set of MAGs using DASTool v1.1.461 with a score threshold of 0.7 for downstream analyses,
711 and those with a minimum completion of 90% and less than 5% contamination as assessed by CheckM
712 v1.1.3. Taxonomy was assigned to the MAGs using the extensive database packaged with gtdbtk v2.0.1.
713 For the analyses of functional potential from the assembled contigs, open-reading frames were predicted
714 from contigs using a modified version of Prokka that includes Prodigal gene predictions for complete and
715 incomplete open-reading frames. The identified genes were annotated with a hidden Markov models
716 (HMM) approach, trained using an in-house database including KOs derived from the Kyoto Encyclopedia
717 of Genes and Genomes (KEGG)[65–67], Pfam[68] and dbCAN[69] databases. All downstream analyses using the
718 files obtained via IMP were performed in R (version 4.2.2) using RStudio (version 2022.07.2). Differential
719 analysis was performed using the package *DESeq2*, microbial community analyses including non-metric
720 dimensional scaling (NMDS) analyses were performed using the R package *vegan* (version 2.6-4)[70]. For
721 further functional analysis as well as graphical representation R packages [59] *enhancedVolcano* (version
722 1.16.0)[71], *clusterProfiler*[72], *ggplot2*[73], *ggpubr* (version 0.6.0)[74], *tidyverse*[75] and *RColorBrewer* (version 1.1-
723 3)[76] were used. Details on the workflows and RMarkdowns can be found on
724 https://gitlab.lcsb.uni.lu/mdm/tsenkova_et_al_2024/.
725
726 *Metabolomic profiling data pre-processing of untargeted LC-MS datasets*
727 Raw data files obtained through LC-MS of human stool and murine plasma and stool samples were
728 processed in TraceFinder (version 5.1.203.0) for peak identification and annotation. Three different in-
729 house libraries, generated with reference standards, as well as one commercially available library,
730 mzCloud Offline for mzVault 2.3_Omics_2020A.db, in the Advanced Mass Spectral Database (AMSD)
731 (HighChem, from ThermoFischer Scientific), were used for peak annotation, with the adduct formulas
732 $[M+H]^+$ and $[M-H]^-$. Annotated features and integration tables were exported for post-processing.

733 *Metabolomic profiling data pre-processing of untargeted GC-MS datasets*

734 Raw data files obtained through GC-MS murine plasma and stool samples were processed in
735 MetaboliteDetector[77] (version 3. 220190704) for peak identification and annotation. An in-house library,
736 generated with reference standards was used for peak annotation. Deconvolution settings were applied
737 as follows: peak threshold = 5, minimum peak height = 5, bins per scan = 10, deconvolution width = 5
738 scans, no baseline adjustment, minimum 15 peaks per spectrum and no minimum required base peak
739 intensity. The data was normalized using the response ratio of the integrated peak area of each metabolite
740 and the integrated peak area of the IS, as described in[78]. Annotated features and integration tables were
741 exported for post-processing.

742

743 *Metabolomic profiling post-processing data analysis*

744 For murine plasma metabolites identified in the SPF experiment (Extended Data Fig. 4), data was
745 manually curated based on the pooled sample, spiked with the ISM. Features, which could not be
746 confirmed through MS2 data (from the commercially available database[79]) or through the ISM were
747 filtered out. Metabolites with missing (N/A) values were also filtered out. Single metabolite intensities
748 were normalized to the total metabolite area and corrected using the mean value of total metabolite
749 values from all samples. LC-MS and GC-MS data were unified, and duplicate metabolites were filtered out,
750 based on reliability and consistency of the peak areas.

751 Human stool sample data was similarly processed (but without the element of data unification
752 between methods).

753 For murine plasma metabolites identified in the GF experiment (GC-MS), metabolites with missing
754 (N/A) values were filtered out.

755 Murine stool SCFA content was quantified based on an IS and using the MassHunter Quantitative
756 Analysis Software (version 10.2.733.8). In the LC-MS and GC-MS datasets, metabolites with over 20%

757 missing (N/A) values were filtered out. Data from murine stool untargeted LC-MS, GC-MS and SCFA
758 quantification was unified and duplicate metabolites were filtered out, based on reliability and
759 consistency of the peak areas.

760 Univariate statistical analysis with Benjamini-Hochberg false discovery rate (BH FDR, performed
761 for all datasets), principal component analysis (PCA), scaling, centering and graphical representation in
762 the form of a heatmap (ComplexHeatmap R package[80]) or log2foldchanges were performed in R version
763 4.2.1 and Rstudio version 1.4.1717. For data scaling and centering, the standard deviation was set to a
764 value of 1 and the mean value was set to 0.

765

766 *Other data analyses*

767 All other data analysis, statistical analysis, and graphical representation, which is not described in
768 the above sections, was performed using Graphpad Prism version 9.4.1.

769

770 *Data availability*

771 Raw sequencing data files for 16S gene sequencing from murine fecal samples are available at the
772 ENA's sequence archive under the accession PRJEB70917 (GF) and PRJEB70920 (SPF). Raw sequencing
773 data files for 16S gene sequencing from human stool samples are available at the ENA's sequence archive
774 under the accession PRJEB70932. Raw sequencing data samples for mouse stool samples are available at
775 the ENA's sequence archive under the accession PRJEB66281. Raw sequencing data files for WGS from
776 human stool samples are available at the ENA's sequence archive under the accession PRJEB70909. Data
777 used to generate the figures are also provided as a 'Source Data' file.

778

779 Additional information regarding experimentation and sample processing can be found in
780 the Supplementary Methods file.

781 **References**

782 1. Colorectal cancer statistics. *WCRF International* https://www.wcrf.org/cancer-trends/colorectal-
783 cancer-statistics/.
784 2. Akimoto, N. *et al.* Rising incidence of early-onset colorectal cancer - a call to action. *Nat. Rev. Clin.*
785 *Oncol.* **18**, 230–243 (2021).
786 3. Weber, D. D. *et al.* Ketogenic diet in the treatment of cancer – Where do we stand? *Mol. Metab.* **33**,
787 102–121 (2019).
788 4. Dmitrieva-Posocco, O. *et al.* β-Hydroxybutyrate suppresses colorectal cancer. *Nature* **605**, 160–165
789 (2022).
790 5. Ang, Q. Y. *et al.* Ketogenic Diets Alter the Gut Microbiome Resulting in Decreased Intestinal Th17
791 Cells. *Cell* **181**, 1263-1275.e16 (2020).
792 6. Kong, C. *et al.* Ketogenic diet alleviates colitis by reduction of colonic group 3 innate lymphoid cells
793 through altering gut microbiome. *Signal Transduct. Target. Ther.* **6**, 154 (2021).
794 7. Wei, R. *et al.* Ketogenesis Attenuates KLF5-Dependent Production of CXCL12 to Overcome the
795 Immunosuppressive Tumor Microenvironment in Colorectal Cancer. *Cancer Res.* **82**, 1575–1588
796 (2022).
797 8. Ferrere, G. *et al.* Ketogenic diet and ketone bodies enhance the anticancer effects of PD-1 blockade.
798 *JCI Insight* **6**, 145207 (2021).
799 9. Wong, C. C. & Yu, J. Gut microbiota in colorectal cancer development and therapy. *Nat. Rev. Clin.*
800 *Oncol.* **20**, 429–452 (2023).
801 10. El Tekle, G. & Garrett, W. S. Bacteria in cancer initiation, promotion and progression. *Nat. Rev.*
802 *Cancer* **23**, 600–618 (2023).
803 11. Paoli, A. *et al.* Ketogenic Diet and Microbiota: Friends or Enemies? *Genes* **10**, 534 (2019).

804 12. Cairo, C. & Webb, T. J. Effective Barriers: The Role of NKT Cells and Innate Lymphoid Cells in the Gut.
805 *J. Immunol. Baltim. Md 1950* **208**, 235–246 (2022).
806 13. Jukic, A., Bakiri, L., Wagner, E. F., Tilg, H. & Adolph, T. E. Calprotectin: from biomarker to biological
807 function. *Gut* **70**, 1978–1988 (2021).
808 14. Wong, S. H. *et al.* Gavage of Fecal Samples From Patients With Colorectal Cancer Promotes
809 Intestinal Carcinogenesis in Germ-Free and Conventional Mice. *Gastroenterology* **153**, 1621-1633.e6
810 (2017).
811 15. Mu, C. *et al.* Probiotics counteract hepatic steatosis caused by ketogenic diet and upregulate AMPK
812 signaling in a model of infantile epilepsy. *EBioMedicine* **76**, 103838 (2022).
813 16. Nan, F. *et al.* Mannose: A Sweet Option in the Treatment of Cancer and Inflammation. *Front.*
814 *Pharmacol.* **13**, (2022).
815 17. Gonzalez, P. S. *et al.* Mannose impairs tumour growth and enhances chemotherapy. *Nature* **563**,
816 719–723 (2018).
817 18. Liu, Q., Li, X., Zhang, H. & Li, H. Mannose Attenuates Colitis-Associated Colorectal Tumorigenesis by
818 Targeting Tumor-Associated Macrophages. *J. Cancer Prev.* **27**, 31–41 (2022).
819 19. De Simone, V., Pallone, F., Monteleone, G. & Stolfi, C. Role of TH17 cytokines in the control of
820 colorectal cancer. *Oncoimmunology* **2**, e26617 (2013).
821 20. Ternes, D. *et al.* Microbiome in Colorectal Cancer: How to Get from Meta-omics to Mechanism?
822 *Trends Microbiol.* **28**, 401–423 (2020).
823 21. Fan, L. *et al.* A. Muciniphila Suppresses Colorectal Tumorigenesis by Inducing TLR2/NLRP3-Mediated
824 M1-Like TAMs. *Cancer Immunol. Res.* **9**, 1111–1124 (2021).
825 22. Wardman, J. F., Bains, R. K., Rahfeld, P. & Withers, S. G. Carbohydrate-active enzymes (CAZymes) in
826 the gut microbiome. *Nat. Rev. Microbiol.* **20**, 542–556 (2022).

827 23. Han, S. *et al.* A metabolomics pipeline for mechanistic interrogation of the gut microbiome. *Nature*
828 **595**, 415–420 (2021).
829 24. Mao, T. *et al.* Elevated serum β-hydroxybutyrate, a circulating ketone metabolite, accelerates
830 colorectal cancer proliferation and metastasis via ACAT1. *Oncogene* **42**, 1889–1899 (2023).
831 25. Gopalakrishnan, V. *et al.* Gut microbiome modulates response to anti-PD-1 immunotherapy in
832 melanoma patients. *Science* **359**, 97–103 (2018).
833 26. Matson, V. *et al.* The commensal microbiome is associated with anti-PD-1 efficacy in metastatic
834 melanoma patients. *Science* **359**, 104–108 (2018).
835 27. Routy, B. *et al.* Gut microbiome influences efficacy of PD-1-based immunotherapy against epithelial
836 tumors. *Science* **359**, 91–97 (2018).
837 28. Olson, C. A. *et al.* The Gut Microbiota Mediates the Anti-Seizure Effects of the Ketogenic Diet. *Cell*
838 **173**, 1728-1741.e13 (2018).
839 29. cis-Encoded Small RNAs, a Conserved Mechanism for Repression of Polysaccharide Utilization in
840 Bacteroides | Journal of Bacteriology. https://journals.asm.org/doi/10.1128/jb.00381-16.
841 30. Pudlo, N. A. *et al.* Symbiotic Human Gut Bacteria with Variable Metabolic Priorities for Host Mucosal
842 Glycans. *mBio* **6**, 10.1128/mbio.01282-15 (2015).
843 31. Milani, C. *et al.* Bifidobacteria exhibit social behavior through carbohydrate resource sharing in the
844 gut. *Sci. Rep.* **5**, 15782 (2015).
845 32. Luis, A. S. & Hansson, G. C. Intestinal mucus and their glycans: A habitat for thriving microbiota. *Cell*
846 *Host Microbe* **31**, 1087–1100 (2023).
847 33. Drula, E. *et al.* The carbohydrate-active enzyme database: functions and literature. *Nucleic Acids*
848 *Res.* **50**, D571–D577 (2022).
849 34. Desai, M. S. *et al.* A dietary fiber-deprived gut microbiota degrades the colonic mucus barrier and
850 enhances pathogen susceptibility. *Cell* **167**, 1339-1353.e21 (2016).

851 35. van der Lugt, B. *et al.* Akkermansia muciniphila ameliorates the age-related decline in colonic mucus
852 thickness and attenuates immune activation in accelerated aging Ercc1−/Δ7 mice. *Immun. Ageing*
853 **16**, 6 (2019).
854 36. Gamage, H. K. A. H. *et al.* Changes in dietary fiber intake in mice reveal associations between colonic
855 mucin O-glycosylation and specific gut bacteria. *Gut Microbes* **12**, 1802209 (2020).
856 37. Johansson, M. E. V. *et al.* Normalization of Host Intestinal Mucus Layers Requires Long-Term
857 Microbial Colonization. *Cell Host Microbe* **18**, 582–592 (2015).
858 38. Brown, E. M., Clardy, J. & Xavier, R. J. Gut microbiome lipid metabolism and its impact on host
859 physiology. *Cell Host Microbe* **31**, 173–186 (2023).
860 39. Yamada, S. *et al.* Gut microbiota-mediated generation of saturated fatty acids elicits inflammation in
861 the liver in murine high-fat diet-induced steatohepatitis. *BMC Gastroenterol.* **17**, 136 (2017).
862 40. Guillou, H., Zadravec, D., Martin, P. G. P. & Jacobsson, A. The key roles of elongases and desaturases
863 in mammalian fatty acid metabolism: Insights from transgenic mice. *Prog. Lipid Res.* **49**, 186–199
864 (2010).
865 41. Yao, J. & Rock, C. O. Exogenous fatty acid metabolism in bacteria. *Biochimie* **141**, 30–39 (2017).
866 42. Flowers, M. T. & Ntambi, J. M. Role of stearoyl-coenzyme A desaturase in regulating lipid
867 metabolism. *Curr. Opin. Lipidol.* **19**, 248–256 (2008).
868 43. Lien, E. C. *et al.* Low glycaemic diets alter lipid metabolism to influence tumour growth. *Nature* **599**,
869 302–307 (2021).
870 44. Zhou, X. *et al.* Stearoyl-CoA Desaturase-Mediated Monounsaturated Fatty Acid Availability Supports
871 Humoral Immunity. *Cell Rep.* **34**, (2021).
872 45. Grajchen, E. *et al.* Fatty acid desaturation by stearoyl-CoA desaturase-1 controls regulatory T cell
873 differentiation and autoimmunity. *Cell. Mol. Immunol.* **20**, 666–679 (2023).

874 46. Kindt, A. *et al.* The gut microbiota promotes hepatic fatty acid desaturation and elongation in mice.
875 *Nat. Commun.* **9**, 3760 (2018).
876 47. Kim, K. S. *et al.* Genome-wide multi-omics analysis reveals the nutrient-dependent metabolic
877 features of mucin-degrading gut bacteria. *Gut Microbes* **15**, 2221811 (2023).
878 48. McKain, N., Shingfield, K. J. & Wallace, R. J. Metabolism of conjugated linoleic acids and 18 : 1 fatty
879 acids by ruminal bacteria: products and mechanisms. *Microbiology* **156**, 579–588 (2010).
880 49. Microbial Production of Conjugated Linoleic Acid and Conjugated Linolenic Acid Relies on a
881 Multienzymatic System | Microbiology and Molecular Biology Reviews.
882 https://journals.asm.org/doi/10.1128/mmbr.00019-18.
883 50. Fermor, B. F. *et al.* Fatty acid composition of normal and malignant cells and cytotoxicity of stearic,
884 oleic and sterculic acids in vitro. *Eur. J. Cancer Oxf. Engl. 1990* **28A**, 1143–1147 (1992).
885 51. Habib, N. A. *et al.* Stearic acid and carcinogenesis. *Br. J. Cancer* **56**, 455–458 (1987).
886 52. Evans, L. M., Cowey, S. L., Siegal, G. P. & Hardy, R. W. Stearate preferentially induces apoptosis in
887 human breast cancer cells. *Nutr. Cancer* **61**, 746–753 (2009).
888 53. Mitchel, J. *et al.* Computational Identification of Stearic Acid as a Potential PDK1 Inhibitor and In
889 Vitro Validation of Stearic Acid as Colon Cancer Therapeutic in Combination with 5-Fluorouracil.
890 *Cancer Inform.* **20**, 11769351211065979 (2021).
891 54. Zhang, Y. *et al.* Altered gut microbiome composition in children with refractory epilepsy after
892 ketogenic diet. *Epilepsy Res.* **145**, 163–168 (2018).
893 55. Naqash, A. R. *et al.* The role of gut microbiome in modulating response to immune checkpoint
894 inhibitor therapy in cancer. *Ann. Transl. Med.* **9**, 1034 (2021).
895 56. Varrette, S., Bouvry, P., Cartiaux, H. & Georgatos, F. Management of an academic HPC cluster: The
896 UL experience. in *2014 International Conference on High Performance Computing & Simulation*
897 *(HPCS)* 959–967 (IEEE, Bologna, Italy, 2014). doi:10.1109/HPCSim.2014.6903792.

898 57. Callahan, B. J. *et al.* DADA2: High-resolution sample inference from Illumina amplicon data. *Nat.*
899 *Methods* **13**, 581–583 (2016).
900 58. Lin, H. & Peddada, S. D. Analysis of microbial compositions: a review of normalization and
901 differential abundance analysis. *Npj Biofilms Microbiomes* **6**, 1–13 (2020).
902 59. Anders, S. & Huber, W. Differential expression analysis for sequence count data. *Genome Biol.* **11**,
903 R106 (2010).
904 60. phyloseq: An R Package for Reproducible Interactive Analysis and Graphics of Microbiome Census
905 Data | PLOS ONE. https://journals.plos.org/plosone/article?id=10.1371/journal.pone.0061217.
906 61. Clarke, E. L. *et al.* Sunbeam: an extensible pipeline for analyzing metagenomic sequencing
907 experiments. *Microbiome* **7**, 46 (2019).
908 62. Integrating taxonomic, functional, and strain-level profiling of diverse microbial communities with
909 bioBakery 3 | eLife. https://elifesciences.org/articles/65088.
910 63. Narayanasamy, S. *et al.* IMP: a pipeline for reproducible reference-independent integrated
911 metagenomic and metatranscriptomic analyses. *Genome Biol.* **17**, 260 (2016).
912 64. Hickl, O., Queirós, P., Wilmes, P., May, P. & Heintz-Buschart, A. binny: an automated binning
913 algorithm to recover high-quality genomes from complex metagenomic datasets. *Brief. Bioinform.*
914 **23**, bbac431 (2022).
915 65. Kanehisa, M. & Goto, S. KEGG: Kyoto Encyclopedia of Genes and Genomes. *Nucleic Acids Res.* **28**,
916 27–30 (2000).
917 66. Kanehisa, M., Furumichi, M., Sato, Y., Kawashima, M. & Ishiguro-Watanabe, M. KEGG for taxonomy-
918 based analysis of pathways and genomes. *Nucleic Acids Res.* **51**, D587–D592 (2023).
919 67. Kanehisa, M. Toward understanding the origin and evolution of cellular organisms. *Protein Sci.* **28**,
920 1947–1951 (2019).

921 68. Mistry, J. *et al.* Pfam: The protein families database in 2021. *Nucleic Acids Res.* **49**, D412–D419
922 (2021).
923 69. Yin, Y. *et al.* dbCAN: a web resource for automated carbohydrate-active enzyme annotation. *Nucleic*
924 *Acids Res.* **40**, W445-451 (2012).
925 70. Oksanen, J. *et al.* vegan: Community Ecology Package. (2022).
926 71. Blighe, K. *et al.* EnhancedVolcano: Publication-ready volcano plots with enhanced colouring and
927 labeling. Bioconductor version: Release (3.18) https://doi.org/10.18129/B9.bioc.EnhancedVolcano
928 (2023).
929 72. Wu, T. *et al.* clusterProfiler 4.0: A universal enrichment tool for interpreting omics data. *Innov.*
930 *Camb. Mass* **2**, 100141 (2021).
931 73. ggplot2: Elegant Graphics for Data Analysis (3e). https://ggplot2-book.org/.
932 74. Kassambara, A. ggpubr: 'ggplot2' Based Publication Ready Plots. (2023).
933 75. Wickham, H. *et al.* Welcome to the Tidyverse. *J. Open Source Softw.* **4**, 1686 (2019).
934 76. Neuwirth, E. RColorBrewer: ColorBrewer Palettes. (2022).
935 77. Hiller, K. *et al.* MetaboliteDetector: comprehensive analysis tool for targeted and nontargeted
936 GC/MS based metabolome analysis. *Anal. Chem.* **81**, 3429–3439 (2009).
937 78. De Saedeleer, B. *et al.* Systematic characterization of human gut microbiome-secreted molecules by
938 integrated multi-omics. *ISME Commun.* **1**, 1–6 (2021).
939 79. Xue, J., Guijas, C., Benton, H. P., Warth, B. & Siuzdak, G. METLIN MS2 molecular standards database:
940 a broad chemical and biological resource. *Nat. Methods* **17**, 953–954 (2020).
941 80. Gu, Z., Eils, R. & Schlesner, M. Complex heatmaps reveal patterns and correlations in
942 multidimensional genomic data. *Bioinformatics* **32**, 2847–2849 (2016).
943